JM PAPERS

Refraction of a triple-shock configuration at planar fast–slow gas interfaces

Enlai Zhang[1]**, Shenfei Liao**[1]**, Liyong Zou**[1,†]**, Zhigang Zhai**[2,†]**, Jinhong Liu**[1]** and Xinzhu Li**[1]

[1]National Key Laboratory of Shock Wave and Detonation Physics, Institute of Fluid Physics, China Academy of Engineering Physics, Mianyang 621900, PR China

[2]Advanced Propulsion Laboratory, Department of Modern Mechanics, University of Science and Technology of China, Hefei 230026, PR China

This paper characterizes the refraction of a triple-shock configuration at planar fast–slow gas interfaces. The primary objective is to reveal the wave configurations and elucidate the mechanisms governing circulation deposition and velocity perturbation on the interface caused by triple-shock refraction. The incident triple-shock configuration is generated by diffracting a planar shock around a rigid cylinder, and four interfaces with various Z_r (i.e. acoustic impedance ratio across the interface) are considered. An analytical model describing the triple-shock refraction is developed, which accurately predicts both the wave configurations as well as circulation deposition and velocity perturbation. Depending on Z_r, three distinct patterns of transmitted waves can be anticipated: a triple-shock configuration; a four-shock configuration; a four-wave configuration. The underlying mechanism for the formation of these wave configurations is elucidated through shock polar analysis. A novel physical insight into the contribution of triple-shock refraction to the interface perturbation growth is provided. The results indicate that the reflected shock in an incident triple-shock configuration makes significant negative contribution to both circulation deposition and velocity perturbation. This investigation elucidates the underlying mechanism responsible for the relatively insignificant contribution of baroclinic circulation to the Richtmyer–Meshkov-like instability induced by a non-uniform shock, and provides an explanation for the decrease in growth rate of interface perturbation amplitude with increasing Atwood number.

Key words: shock waves

† Email addresses for correspondence: zly@caep.cn, sanjing@ustc.edu.cn

E. Zhang, S. Liao, L. Zou, Z. Zhai, J. Liu and X. Li

1. Introduction

Shock refraction and reflection occur simultaneously when a shock wave encounters an interface separating two fluids with different thermal properties. As a canonical problem in compressible hydrodynamics, shock refraction has long been a fascinating research topic due to its fundamental significance in scientific research, as well as its crucial role in natural phenomena (Arnett, Bahcall & Kirshner 1989) and engineering applications including inertial confinement fusion (ICF) (Lindl *et al.* 2004; Betti & Hurricane 2016) and supersonic combustion (Yang, Kubota & Zukoski 1994; Ren *et al.* 2019). One of the first theoretical investigations on shock refraction was carried out by Taub (1947) and Polachek & Seeger (1951), who independently formulated a theoretical description of the regular refraction phenomenon that occurs when a planar shock wave encounters an inclined gaseous interface. Shock tube experiments were then performed by Jahn (1956) to study the refraction of planar shock waves at the inclined air–CH$_4$ and air–CO$_2$ interfaces, respectively, and several irregular shock refraction patterns were observed and discussed. Subsequently, understanding the underlying flow physics governing these shock refraction phenomena and their impacts on interface evolution has been a longstanding research focus. By utilizing a combination of theoretical analysis (Henderson 1966, 1989, 2014), experimental investigations (Abd-El-Fattah, Henderson & Lozzi 1976; Abd-El-Fattah & Henderson 1978*a,b*; Zhai *et al.* 2017) and numerical simulations (Nourgaliev *et al.* 2005; Xiang & Wang 2019; de Gouvello *et al.* 2021), the three dominant factors determining the pattern of shock refraction have been identified. These factors include the acoustic impedances of the fluids on either side of the interface, the angle of incidence of the shock wave onto the interface, and the strength of the incident shock (Nourgaliev *et al.* 2005). Also, a theoretical shock refraction regime diagram taking these factors into account has been established by shock polar analysis (Abd-El-Fattah & Henderson 1978*a,b*; de Gouvello *et al.* 2021). While the aforementioned studies primarily focused on gaseous interfaces, investigations of shock refraction have been extended to more complex regimes involving solid materials (Brown & Ravichandran 2014), liquids (Wan *et al.* 2017; Xiang & Wang 2019) and plasmas (Li, Samtaney & Wheatley 2018; Pellone *et al.* 2021).

During shock refraction, due to misalignment of the pressure with density gradients, baroclinic vorticity is deposited on the interface. After the passage of the shock, the interface undergoes persistent deformation, which may lead to turbulent mixing (Zhou 2017*a,b*). This phenomenon is known as Richtmyer–Meshkov instability (RMI), named after the pioneering contributions of Richtmyer (1960) and Meshkov (1969). The primary driver of perturbation growth is the localized vorticity deposited on the interface through shock refraction (Brouillette 2002; Peng, Zabusky & Zhang 2003; Nishihara *et al.* 2010; Zhou 2017*a*; Peng *et al.* 2021). Hawley & Zabusky (1989) first qualitatively described the evolution of RMI from the perspective of vorticity dynamics and introduced a vorticity paradigm which involves four distinct phases: the vorticity deposition phase; the linear and early nonlinear phase; the intermediate nonlinear phase; the late time phase. The vorticity deposition phase is crucial for RMI as it dominates the subsequent flow evolution (Zabusky 1999; Peng *et al.* 2021; Hong *et al.* 2022). Consequently, accurate prediction of vorticity generation in RMI environments has become a fascinating focus of research. The first quantitative investigation of vorticity generation in shock-planar interface interaction was presented by Yang *et al.* (1992). Subsequently, using shock polar analysis, Samtaney & Zabusky (1994) derived an analytical expression for the circulation deposited on an inclined fast–slow interface (i.e. when a shock propagates from a medium with low acoustic impedance to one with high acoustic impedance), which is commonly referred to as the SZ model. The SZ model has been successfully applied to interfaces of various
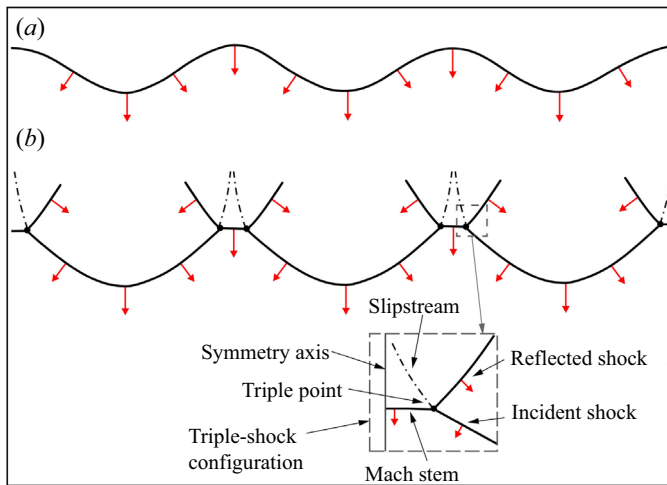
Figure 1. Schematic diagram of non-uniform shocks: (*a*) a non-uniform shock with a smooth shock front; (*b*) a faceted non-uniform shock with inherent triple-shock configurations. The red arrows indicate the orientations of the shocks.

geometries, including circular (Li, Guan & Wang 2022*b*), sinusoidal (Li *et al.* 2022*a*) and elliptical ones (Li, Wang & Guan 2019). Recently, Liu *et al.* (2020) considered the contribution of viscosity to the circulation deposition in RMI and argued that the viscosity gradient inside the shocks plays a role in the circulation deposition.

Previous works on shock refraction and RMI have mainly dealt with uniform incident shocks, perfectly planar or cylindrical. However, in practical applications, the incident shocks exhibit inherent non-uniformity and propagate with oscillations, giving rise to the spontaneous emergence of geometric singularities such as triple points and Mach stems (Gardner, Book & Bernstein 1982; Lodato, Vervisch & Clavin 2016; Mostert *et al.* 2018*a*,*b*), as depicted in figure 1. Upon encountering an interface, these non-uniform incident shocks inevitably seed perturbations that are subsequently amplified, even if the interface is initially uniform (Ishizaki & Nishihara 1997; Smalyuk *et al.* 2020; Velikovich *et al.* 2020). For instance, in the context of ICF, non-uniform laser illumination launches a non-spherical shock wave that undergoes a nonlinear transition, resulting in the formation of a faceted polyhedral shock consisting of incident shocks, triple points, Mach stems, and following reflected polar shocks (Gardner *et al.* 1982; Thomas & Kares 2012). This faceted, non-uniform shock seeds perturbations for the acceleration phase of the target, inducing Rayleigh–Taylor instability and facilitating turbulent mixing that ultimately results in ignition failure (Thomas & Kares 2012; Smalyuk *et al.* 2020). Such interactions are complicated and it is imperative to conduct exploratory studies in order to elucidate the crucial processes involved.

Ishizaki *et al.* (1996) first numerically investigated the instability of a uniform interface accelerated by a non-uniform shock driven by a moving rippled piston. They reported that the evolution of this instability exhibits two distinct regimes, namely linear and nonlinear regimes, depending on the amplitude of the rippled piston. The linear regime occurs when the amplitude of the rippled piston is small and the non-uniform shock front is sinusoidal (see figure 1*a*). For this regime, Ishizaki *et al.* (1996) proposed an analytical theory that considers both the impulsive acceleration induced by the non-uniform shock front and the continuous pressure perturbation behind the shock front. However, when the amplitude of the rippled piston increases, the initially sinusoidal shock front undergoes

a transition to a faceted one characterized by 'cusp-like structured shock' (i.e. triple points and Mach stems) (see figure 1*b*). This phenomenon indicates the emergence of a nonlinear regime, which is characterized by the formation of irregular square-shaped perturbations on the interface. It was inferred that these square-shaped perturbations are induced by velocity impulses resulting from the passage of the 'cusp-like structured shocks'. Such instabilities induced by non-uniform shocks are commonly referred to as Richtmyer–Meshkov-like (RM-like) instability in the literature (Velikovich 2000; Nishihara *et al.* 2010). Our recent shock tube experiments (Zou *et al.* 2017) have also examined the RM-like instability, where a non-uniform shock with inherent triple-shock configurations is produced by diffracting a planar shock around a rigid cylinder. Of great interest, the incident triple-shock configuration imprints a central cavity on the interface, which exhibits a morphology similar to the square-shaped perturbations previously observed by Ishizaki *et al.* (1996). Subsequently, Zhou (2017*a*) has specially addressed this RM-like instability in his review article. More recently, Liao *et al.* (2019) experimentally examined the effects of the Atwood number (defined as $At = (\rho_{0'} - \rho_0)/(\rho_{0'} + \rho_0)$ with ρ_0 and $\rho_{0'}$ being the initial densities of the light and heavy gases, respectively) on the perturbation growth of this RM-like instability. They concluded that the perturbation growth rate of this RM-like instability decreases as the Atwood number increases, which is fundamentally different from the results related to the classical RMI. However, the underlying physical mechanism behind this novel phenomenon remains unclear (He *et al.* 2023).

The aforementioned investigations have provided valuable insights into the flow physics of the RM-like instability. However, a comprehensive analytical theory that accounts for the scenarios of RM-like instability has yet to be developed due to the complexity introduced by triple-shock configurations. As depicted in figure 1(*b*), a triple-shock configuration consists of four discontinuities, namely a Mach stem, incident and reflected shocks, and a slipstream. The leading shock front comprises the Mach stem and incident shock, while the reflected shock originates from the triple point and travels transversely behind it (Lau-Chapdelaine & Radulescu 2016). When a triple-shock configuration encounters an interface, both the leading shock front and the reflected shock successively interact with the interface. These interactions inevitably give rise to complex wave configurations and deposit velocity perturbations as well as baroclinic vorticity on the interface. Therefore, accurately predicting the velocity perturbation and vorticity deposition induced by triple-shock refraction is of great significance in uncovering the underlying physical mechanisms governing the RM-like instability. In addition, it is of great interest and importance to understand the wave configuration that occurs when a triple-shock configuration refracts at a planar interface. A definite answer to these questions requires a detailed and careful examination of the triple-shock refraction process, which motivates this work. The remainder of the paper is organized as follows. The numerical approach, experimental set-up and analytical method are presented in § 2. Detailed results and discussion regarding the flow features are provided in §§ 3 and 4. Finally, concluding remarks are summarized in § 5.

2. Methodology

According to our previous works (Zou *et al.* 2017; Liao *et al.* 2019), the incident triple-shock configuration is generated by diffracting a planar shock around a rigid cylinder. As indicated by Bryson & Gross (1961) and Zou *et al.* (2017), the structure of the incident triple-shock configuration is determined by the Mach number of the

incident planar shock, the diameter of the rigid cylinder, together with the distance that the diffracted shock travels downstream. In the present work, to eliminate the complexity induced by the variation of the structure of the incident triple-shock configuration, the Mach number of the incident planar shock is kept at $M_i = 1.80$, the diameter of the rigid cylinder is kept at $d = 10$ mm and the distance between the centre of the rigid cylinder and the initial interface is kept at $l = 40$ mm.

2.1. *Numerical approach*

The numerical simulations are conducted using a compressible multicomponent Euler solver based on the finite volume method (Sun & Takayama 1999). In a quasiconservative form, the governing equations can be written as

$$\frac{\partial U}{\partial t} + \frac{\partial F(U)}{\partial x} + \frac{\partial G(U)}{\partial y} = 0, \tag{2.1}$$

where U represents the conserved variable, $F(U)$ and $G(U)$ are the convective fluxes in the x and y directions, respectively,

$$U = \begin{pmatrix} \rho \\ \rho u \\ \rho v \\ \rho E \\ \rho Y_s \end{pmatrix}, \quad F = \begin{pmatrix} \rho u \\ \rho u^2 + p \\ \rho uv \\ (\rho E + p)u \\ \rho Y_s u \end{pmatrix}, \quad G = \begin{pmatrix} \rho v \\ \rho uv \\ \rho v^2 + p \\ (\rho E + p)v \\ \rho Y_s v \end{pmatrix}, \tag{2.2a–c}$$

where u and v represent the velocity components in the x and y directions, respectively, and ρ and p represent the density and pressure. Here Y_s stands for the mass fraction of the gas at one side of the interface, and the mass fraction of gas b at the other side of the interface is $Y_b = 1 - Y_s$. The equation of state of the mixture is expressed as $p = \rho T (Y_s R_s + Y_b R_b)$, where R_s and R_b are the gas constants of gases s and b, and T is the temperature of the mixture. Here E is the total energy of the mixture, defined as $E = Y_s e_s + Y_b e_b + (u^2 + v^2)/2$ where e_s and e_b are the internal energies of gases s and b.

The MUSCL (monotonic upstream-centred scheme for conservation laws)–Hancock scheme (Toro 2009) is adopted to achieve the second-order accuracy in both temporal and spatial scales. The HLL (Harten–Lax–van Leer) Riemann solver (Sun & Takayama 2003) is employed for the approximation of the physical fluxes. An adaptive mesh refinement technique (Sun & Takayama 1999) is employed such that it deploys dense grids in flow regions with large density and velocity gradients, thereby resolving waves and interface evolutions elaborately. This solver has been proven reliable in previous works in capturing the complex shock structures and interface evolution, such as shock–obstacle interactions (Sun & Takayama 2003), shock reflections (Wang & Zhai 2020; Wang, Zhai & Luo 2022) and shock–interface interactions (Zhai *et al.* 2011, 2018).

The computational domain is shown in figure 2(*a*). Due to the symmetric nature of the flow field, only the upper-half-plane ($0 \leqslant x \leqslant 250$ mm and $0 \leqslant y \leqslant 50$ mm) is considered. The rigid cylinder is centred at $x = 20$ mm on the symmetry axis, and the initial interface is situated at $x = 60$ mm. The left and right boundaries are set as inflow and outflow conditions, respectively, while the upper and lower boundaries ($y = 0$ and $y = 50$ mm) are treated as reflection and symmetry conditions, respectively. To highlight the influence of acoustic impedances of the gases on the triple-shock refraction, four different types of fast–slow interfaces are considered in computations with light gas of nitrogen (N_2) and heavy gases of air, carbon dioxide (CO_2), krypton (Kr) and
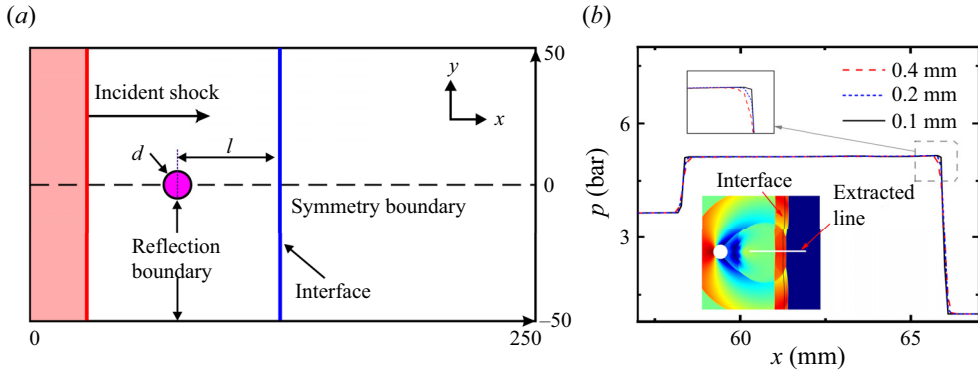
Figure 2. (*a*) Schematic of the computational domain. (*b*) The grid convergence validation.

Case	Gas combination	γ	ρ (kg m^{-3})	a (m s^{-1})	$Z = \rho a$ (kg m^{-2} s^{-1})	Z_r
1	N$_2$–air	1.399	1.204	343.1	413.1	1.02
2	N$_2$–CO$_2$	1.293	1.829	267.6	489.4	1.21
3	N$_2$–Kr	1.661	3.491	220.1	768.4	1.89
4	N$_2$–SF$_6$	1.094	6.143	133.9	822.1	2.02

Table 1. Thermal properties of the test gases considered in the numerical simulations, including the gas combination, specific heat ratio (γ), density (ρ), sound speed (a), acoustic impedance (Z) of the heavy gases at $T_0 = 293.15$ K and $p_0 = 101325$ Pa, and the acoustic impedance ratio (Z_r) across the interface. The value of γ, ρ, a and Z of the light gas (N$_2$) are 1.399, 1.164, 348.9 and 406.1, respectively.

sulphur hexafluoride (SF$_6$), respectively. The thermal properties of the test gases are given in table 1. Here the interfaces are characterized by the acoustic impedance ratios of gases across the interfaces defined as $Z_r = Z_{0'}/Z_0$, with Z_0 and $Z_{0'}$ being the acoustic impedances of the light and heavy gases, respectively.

To validate the numerical solver as well as check the grid convergence, a planar shock diffracting around a rigid cylinder is considered, in which three sets of uniform grids with initial mesh sizes of 0.4, 0.2 and 0.1 mm, respectively, are tested. The initial temperature T_0 of 293.15 K and initial pressure p_0 of 101 325 Pa are employed. The pressure profiles along the horizontal symmetry axis of the flow field with different initial mesh sizes are given in figure 2(*b*). The results obtained by the grids with initial mesh sizes of 0.2 mm and 0.1 mm collapse together, indicating a reasonable convergence of grid resolutions. To ensure the accuracy and meanwhile to minimize the computation capacity, the initial mesh size of 0.2 mm is adopted and the finest mesh size of 25 μm is used where a greater density gradient exists. As depicted in figure 3(*a*), the instantaneous numerical schlieren of the diffracted non-uniform shock just before it encounters the interface is validated against the experimental shadowgraphy of Liao *et al.* (2019). The numerical simulation reproduces nearly all features of wave pattern as observed in the experiment and good agreement is achieved between them. Furthermore, the computed trajectories of the two triple points (TP$_1$, TP$_2$) are measured and compared with the experimental data of Liao *et al.* (2019), as depicted in figure 3(*b*). The comparisons appear substantially satisfactory for both the outer and inner triple-shock configurations, validating the accuracy of the numerical solver.
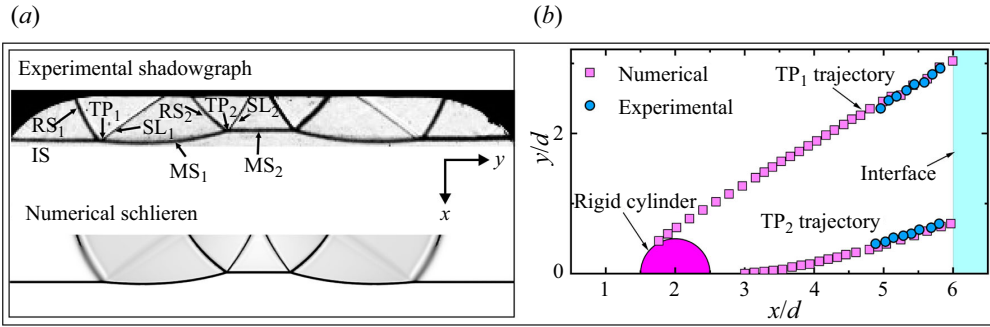
984 A49-6

Figure 3. Validation of the numerical solver. (*a*) Comparison of the wave configuration of the diffracted non-uniform shock just before it encounters the initial interface. (*b*) Comparison of triple points trajectories of the diffracted non-uniform shock.
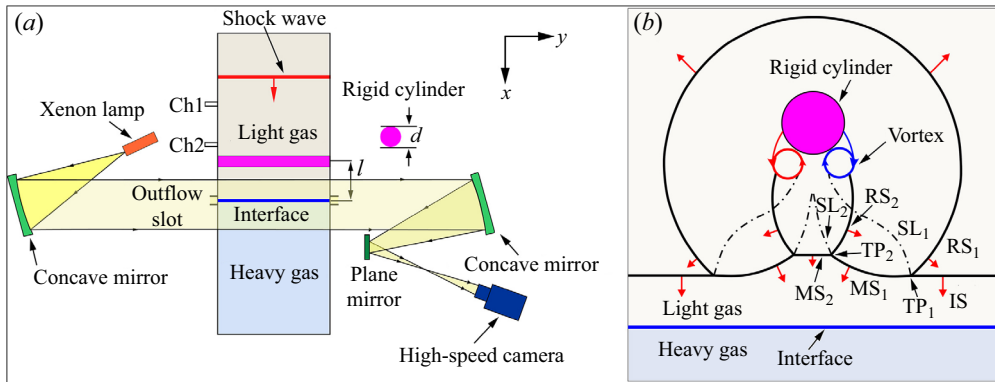

Figure 4. (*a*) Schematic of the test section of the shock tube with shadowgraph system. (*b*) Schematic of wave configurations after the shock diffracts around the cylinder. Here, TP_1 and TP_2, respectively, denote the outer and inner triple points; IS, MS_1, MS_2, RS_1 and RS_2 refer to the incident shock, the outer Mach stem shock, the central Mach stem, the reflected/transverse shock emanating from TP_1 and TP_2, respectively; SL_1 and SL_2 denote the slipstream emanating from TP_1 and TP_2, respectively.

2.2. *Experimental set-up*

The experiments are conducted in a vertical shock tube with a cross-section of 100 mm × 100 mm, comprising of a driver section (1.60 m long), a driven section (4.22 m long), and a test section (0.305 m long). As illustrated in figure 4(*a*), a flat interface is created in the test section utilizing the membraneless method originally proposed by Jones & Jacobs (1997), which has already been verified for its feasibility and reliability in our previous works (Zou *et al.* 2017; Liao *et al.* 2019). The detailed description of the shock tube facility and the interface generation method can be found in Zou *et al.* (2017) and Liao *et al.* (2019). In this work, three different types of fast–slow interfaces are successfully generated with light gas of N_2 and heavy gases of CO_2, Kr and SF_6, respectively. However, the N_2–air interface is excluded in the experiments due to the negligible difference in densities between the two gases, which poses a great challenge for generating the interface. Figure 4(*b*) illustrates the schematic of wave configurations after a planar shock diffracts around a rigid cylinder. To capture the evolution of the wave patterns and the interface elaborately, a shadowgraph photographic system similar to that adopted by Zou *et al.* (2017) and Liao *et al.* (2019) is employed, as shown schematically in figure 4(*a*). A 500 W

xenon lamp (XQW500, Chengdu Photoelectricity Limited) is used to illuminate the flow field, and the shadowgraph images are recorded by a high-speed video camera (Phantom V1610) with a frame rate of 52 000 frames per second. The exposure time of the camera is 1 μs and the spatial resolution of the image is approximately 0.27 mm pixel^{-1}. Two pressure transducers (Ch1, Ch2) located above the test section and spaced 100 mm apart are used to measure the shock speed and to trigger the data acquisition system.

2.3. *Pressure-deflection shock polar*

The utilization of pressure-deflection shock polar is highly advantageous for analysing flow phenomena involving complex shock interactions and shock refractions, thereby facilitating a more comprehensive understanding of the flow physics (Olejniczak, Wright & Candler 1997; Ben-Dor 2007; Vasilev, Elperin & Ben-dor 2008; Gounko 2017; Zhang *et al.* 2021; Bai & Wu 2022). For a detailed description of shock polars and their applications, readers can refer to Ben-Dor (2007). In this study, the triple-shock refraction process is examined by employing shock polars. Moreover, the utilization of shock polars enables a quantitative assessment of the velocity perturbation and the deposition of vorticity during triple-shock refraction (Samtaney & Zabusky 1994). Note that the shock polars and the equations they represent are based on the assumption of a planar shock, which implies a uniform flow immediately downstream. Hence, the shock polars provide only an approximate representation of the actual flow in scenarios involving curved shocks, and are accurate only within a limited region surrounding the point of shock intersection. Nonetheless, based on the numerous numerical and experimental studies performed so far, it seems reasonable to assume a planar shock when using shock polars (Olejniczak *et al.* 1997; Vasilev *et al.* 2008; Gounko 2017; Zhang *et al.* 2021; Ji *et al.* 2022). Therefore, in this study, it is assumed that the shocks of the triple-shock configuration are planar in the vicinity of the triple point, although slight curvature exists.

3. Flow structures and characteristics

3.1. *Features of the diffracted non-uniform shock*

Before illustrating the flow physics of triple-shock refraction, it is necessary to elaborate on the general features of the diffracted non-uniform shock. Diffraction of a planar shock around a rigid cylinder is a classical problem in shock dynamics, and for a detailed analysis readers can refer to Bryson & Gross (1961) and Chaudhuri, Hadjadj & Chinnayya (2011). As shown in figure 4(*a*), the leading shock front of the diffracted non-uniform shock consists of two pairs of triple points (TP$_1$, TP$_2$) and several shock segments, namely the planar incident shock (IS) and the curved Mach stem shocks (MS$_1$, MS$_2$). There are two characteristic triple-shock configurations on both sides of the flow symmetry axis, originating from TP$_1$ and TP$_2$. The structures of the two triple-shock configurations are determined by the Mach number (M) and incidence angle (α, defined as the angle with respect to the horizontal direction) of their leading shock fronts in the vicinity of the triple points. The variation of M and α for each shock segment are extracted from the numerical simulations and presented in figures 5(*a*) and 5(*b*), respectively. The Mach number of MS$_1$ decreases gradually from TP$_1$ to TP$_2$ due to the shock attenuation when diffracting around the cylinder. The Mach number of MS$_2$ exceeds that of MS$_1$ because of the collision of the two MS$_1$ from opposite sides. The incidence angle for IS is maintained at zero. Subsequently, the incidence angle experiences a sudden jump upon crossing TP$_1$ from IS to MS$_1$ due to the shock interaction, then increases monotonically and reaches a local
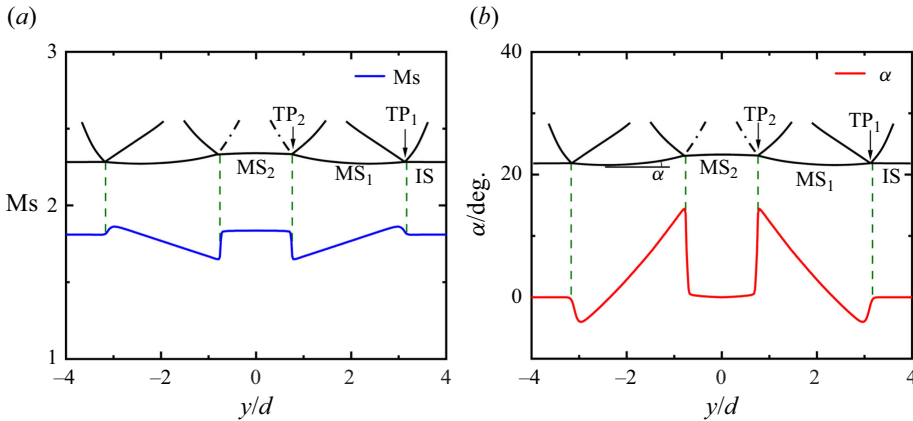
Figure 5. Distribution of (*a*) the Mach number and (*b*) the incidence angle of the leading shock front of the non-uniform shock just before it encounters the initial interface.

maximum value at TP_2. From figure 5, both the shock Mach number and incidence angle exhibit a more pronounced variation when crossing TP_2 compared with TP_1, indicating a stronger and more stable triple-shock configuration originating from TP_2. Therefore, in the subsequent sections, we focus on examining the refraction of the triple-shock configuration originating from TP_2. The shock front parameters depicted in figure 5 will be used as input data for the theoretical analysis, which will be elaborated in detail in § 4.

3.2. *Qualitative description of the triple-shock refraction process*

3.2.1. *Triple-shock refraction at a planar N_2–air interface*

Figure 6 illustrates the refraction of the triple-shock configuration originating from TP_2 at a planar N_2–air interface, where the numerical schlieren images and the schematics of the wave configurations are presented on the left- and right-hand sides, respectively. Due to the symmetric nature of the flow field, only the right-hand half of the entire wave configurations is displayed for clarity. The initial time, i.e. $t = 0$ μs, is defined as the moment when IS collides with the initial interface, and the corresponding wave configuration is shown in figure 6(*a*). As time proceeds, the outer Mach stem shock (MS_1) first intersects the interface at point IP_1 and undergoes primary regular refraction due to its relatively small incidence angle, generating a transmitted shock (TS_1) and a reflected shock (RS_3). A detailed enlargement of the flow field in the vicinity of IP_1, as depicted in figure 6(*b*), reveals that the refraction of MS_1 deposits positive baroclinic vorticity on the interface. At $t = 4$ μs, as shown in figure 6(*c*), the central Mach stem shock (MS_2), the triple point (TP_2) and the outer Mach stem shock (MS_1) all intersect with the interface simultaneously. At this moment, the four shocks RS_2, TS_1, MS_2 and RS_3 coincide at a single point on the interface, mutually modifying each other and indicating a critical condition for the refracting shock system. As presented in figure 4, MS_2 is almost parallel to the initial interface. Consequently, regular refraction of MS_2 occurs upon encountering the initial interface. In conjunction with the refraction of MS_2, RS_2 interferes with RS_3 from the opposite family at point IP_3. This shock interaction generates RS_4 and RS_5 to match the flow field. At the same time, RS_5 intersects with the evolving interface segment previously shocked by MS_1 at point IP_4, resulting in secondary shock refraction and forming a reflected shock (RS_6) and a transmitted shock (TS_2). A zoomed-in view of
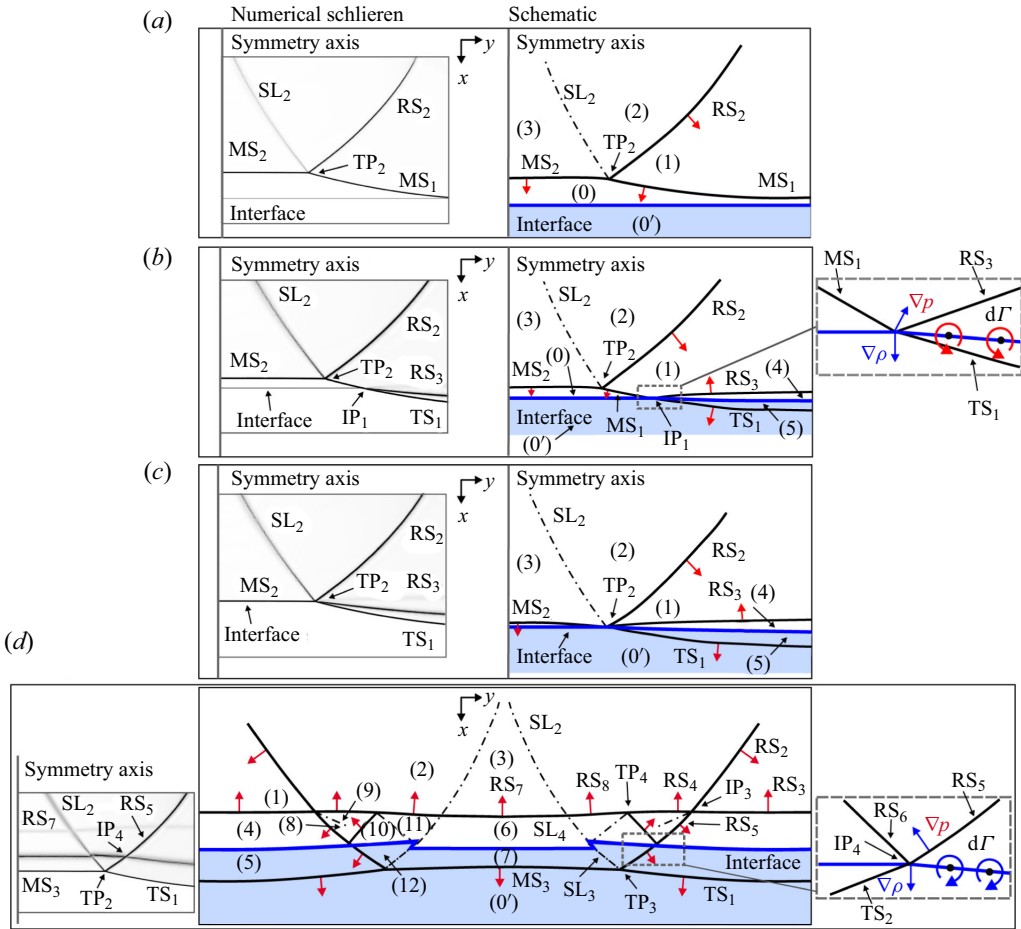
Figure 6. Sequences of numerical schlieren frames and schematic diagrams illustrating the evolution of triple-shock refraction at a N_2–air interface. The red arrows indicate the orientations of the shocks. Here (*a*) $t = 0$ μs, (*b*) $t = 2$ μs, (*c*) $t = 4$ μs and (*d*) $t = 10$ μs.

the flow field near IP_4, as depicted in figure 6(*d*), reveals that the secondary refraction of RS_5 deposits negative vorticity on the interface. That is to say, the secondary refraction of RS_5 suppresses vorticity originally deposited by the primary refraction of MS_1 on the interface.

In addition to the deposition of baroclinic vorticity, the triple-shock refraction also imparts a longitudinal velocity perturbation on the interface. As previously mentioned, the shock Mach number and incidence angle exhibit pronounced variations along the leading shock front of the incident triple-shock configuration, resulting in a non-uniform impulsive acceleration of the interface. Recalling that MS_2 is stronger and has a relatively smaller incidence angle than MS_1 (see figure 5); this implies that the central interface segment shocked by MS_2 immediately gains a larger velocity after the passage of the leading shock front, thereby imparting a velocity perturbation on the interface. However, following the passage of the leading shock front, the secondary refraction of RS_5 at the evolving interface segment shocked by MS_1 further accelerates the interface segment and partially balances the longitudinal velocity perturbation. Consequently, the secondary refraction of RS_5 may effectively suppress the growth of interface perturbation by concurrently

984 A49-10

inhibiting vorticity deposition and balancing velocity perturbations on the interface. Note that in the theoretical analysis of Ishizaki *et al.* (1996), only the velocity perturbation imparted by the leading shock front of a non-uniform shock was considered. However, based on the above results, both the leading shock front and the reflected shock travelling transversely behind it play crucial roles in the interface evolution. The quantitative assessment of the contribution of the reflected shock to the interface evolution will be presented in § 4.3.1.

In concurrence with the perturbation of the interface, a complex pattern of reflected waves is generated, which comprises multiple curved shocks (RS_3, RS_4, RS_7 and RS_8), a triple point (TP_4), a shock intersection point (IP_4) as well as transverse shocks (RS_2, RS_5, RS_6) and slipstreams, as shown in figure 6(*d*). Of great interest, a transmitted triple-shock configuration is identified in the transmitted gas, comprising of shocks TS_1, MS_3, TS_2, as well as a slipstream SL_3 emanating from the transmitted triple point TP_3. For convenience, this type of triple-shock refraction with the formation of a transmitted tripe-shock configuration is referred to as a type A triple-shock refraction.

3.2.2. *Effects of acoustic impedances on the triple-shock refraction*

When Z_r is increased, various patterns of refracted wave configurations are obtained. Figure 7(*a,b*) demonstrates the refractions of the triple-shock configuration at N_2–CO_2 and N_2–Kr interfaces. In general, the evolution of the wave configurations exhibits similar characteristics to those observed in the case of a N_2–air interface, with discrepancies observed only in the transmitted wave configurations as shown in figures 6(*d*) and 7(*a,b*). Notably, the numerical schlieren images shown in figure 7(*a*vi) and 7(*b*vi) clearly display a transmitted four-shock configuration consisting of four shocks (MS_3, TS_1, TS_2 and TS_3) and a slipstream (SL_3). These five discontinuities meet at a single point TP_3, contradicting von Neumann's three-shock theory (Von Neumann 1943, 1945). Note that the discrepancy between von Neumann's three-shock theory and Mach reflection configurations was first experimentally detected by White (1952) in weak shock reflection and subsequently confirmed by numerous experiments (Zaslavsky & Safarov 1975; Henderson & Siegenthaler 1980; Colella & Henderson 1990; Skews & Ashworth 2005). These discrepancies are commonly named the von Neumann paradox. To resolve the von Neumann paradox, Guderley (1947) and Vasilev (1999) developed a four-wave theory by introducing a Prandtl–Meyer expansion fan into the triple-shock configuration. In addition, Vasilev *et al.* (2008) reconsidered the von Neumann paradox using shock polar analysis and predicted two distinct four-wave configurations: Guderley reflection and Vasilev reflection. However, the four-shock configuration identified in this study is distinctly different from the four-wave configurations predicted by Vasilev *et al.* (2008). The shadowgraph images shown in figure 7(*a*v) and 7(*b*v) provide experimental evidence for this four-shock configuration. To the authors' knowledge, such a four-shock configuration has not been reported before. Specifically, this type of triple-shock refraction is referred to as type B triple-shock refraction, and the detailed wave configurations are schematically depicted in figure 8(*a*). Considering the similarity in reflected wave configurations between type A and type B triple-shock refraction, as well as the symmetric nature of the flow field, only the right-hand half of the flow regions within the transmitted gas is illustrated in figure 8(*a*) for clarity.

Regarding the case of N_2–SF_6 interface, the numerical schlieren image presented in figure 7(*c*vi) clearly demonstrates a transmitted four-wave configuration that includes a Prandtl–Meyer expansion fan (EW), in addition to the classical triple-shock configuration. This transmitted four-wave configuration is similar to the wave configuration of both
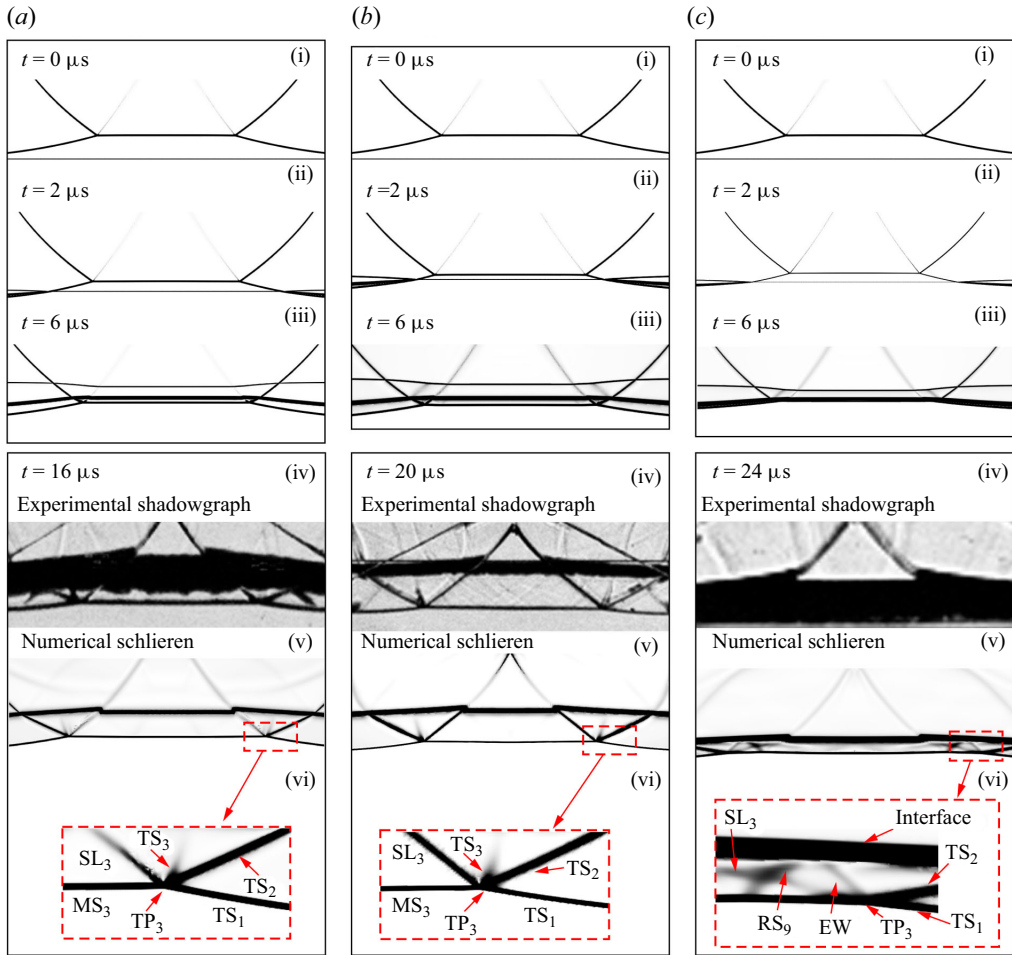
Figure 7. Sequences of numerical schlieren images and experimental shadowgraphs showing the evolution of triple-shock refractions at interfaces with various combinations of acoustic impedances. Here (*a*) N_2/CO_2, (*b*) N_2/Kr and (*c*) N_2/SF_6.
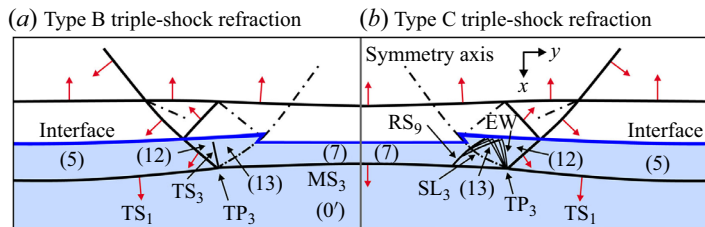

Figure 8. Detailed schematics illustrating the flow field of type B and type C triple-shock refractions.

the Guderley reflection and the Valisev reflection (Vasilev *et al.* 2008). Note that EW originating from TP_3 slightly complicates the flow by impacting the interface in the backward direction and generating a reflected shock RS_9. This type of triple-shock refraction is classified as type C triple-shock refraction. Unfortunately, the experimental identification of the transmitted four-wave configuration is hindered by both the strong

diffusion of the N_2–SF_6 interface and the narrow space between the interface and the transmitted shocks. Figure 8(*b*) illustrates the detailed wave configuration and flow field resulting from type C triple-shock refraction for comparison, highlighting the differences in the flow field near TP_3.

4. Theoretical results and discussion

In this section, analytical models will be developed to solve the wave angles and flow properties behind the waves associated with the process of triple-shock refraction. The input data used in the analytical model includes the parameters of the leading shock front of the incident triple-shock configuration, along with the thermal properties of gases on both sides of the initial interface. Specifically, the analysis decomposed the triple-shock refraction process into five fundamental processes, namely: analytical characterization of the incident triple-shock configuration; solution of the primary shock refraction; solution of the shock–shock interaction; solution of the secondary shock refraction; solution of the transmitted wave configuration. Once the flow properties in different regions illustrated in figures 6(*d*) and 8 have been determined, it becomes feasible to quantitatively evaluate the effects of velocity perturbation and baroclinic vorticity induced by the triple-shock refraction. Moreover, the flow properties of the regions surrounding the transmitted triple point can be utilized to draw shock polars for the transmitted wave configuration, thereby providing valuable insights into the mechanisms that determine the pattern of the transmitted wave.

In the subsequent analysis, we use V and M to represent the velocity and Mach number of the gas, respectively. The angle of the shock wave with respect to its upstream flow direction (shock angle) is denoted by β. The flow deflection angle across a shock or an expansion fan is denoted by δ, with positive values for anticlockwise deflections. The gases are considered as calorically and thermally perfect. The conservation relationships across various types of discontinuities, including oblique shock wave, expansion waves and slipstream, are universal and can be found in Anderson (2001).

4.1. *Analytical solution of the triple-shock refraction*

4.1.1. *Analytical characterization of the incident triple-shock configuration*

The analysis of the triple-shock refraction begins with the characterization of the incident triple-shock configuration. The flow field around TP_2 depicted in figure 4(*a*) is appropriately magnified and presented in figure 9. By attaching a frame of reference to TP_2, the unsteady triple-shock configuration is transformed into a pseudosteady one, and all flow properties that are frame of reference dependent are appropriately marked. Figure 9 shows that four discontinuities, namely MS_1, RS_2, MS_2 and SL_2, coincide at TP_2 and divide the flow field into four regions (i.e. regions (0)–(3)). Similar to von Neumann's three-shock theory (Von Neumann 1945), the flow solutions in regions (0)-(3) are assumed to be uniform, disregarding the influence of shock curvatures. Consequently, the flow field in the vicinity of TP_2 can be solved by applying the conservation relationships across the oblique shocks and appropriate matching conditions across SL_2.

To characterize the incident triple-shock configuration depicted in figure 9(*a*), only three parameters of the leading shock front are required, namely, the Mach numbers (M_i, M_m) of MS_1 and MS_2, along with the incidence angle (α_i) of MS_1. In the frame of reference attached to TP_2, the oncoming flow Mach number ($M_0(TP_2)$) in zone (0) and the shock
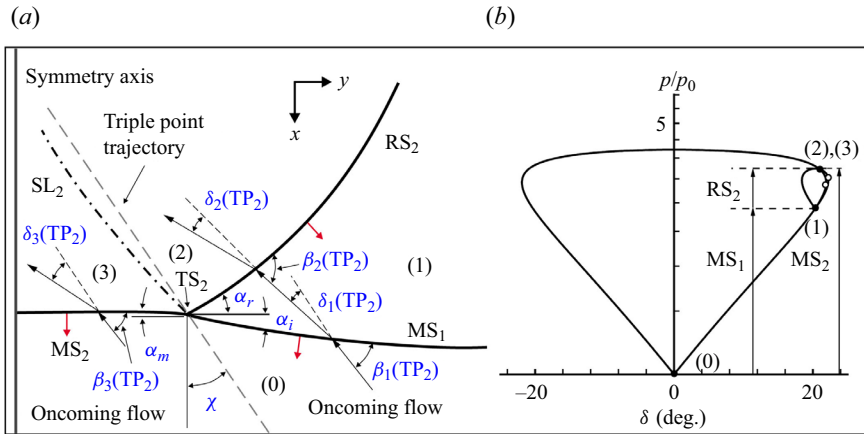
Figure 9. (*a*) Schematic diagram and (*b*) shock-polar solution of the incident triple-shock configuration. The solid points represent the solution points, and the hollow circles denote the sonic points.

angle ($\beta_i(\mathrm{TP}_2)$) of MS_1 are derived as

$$\left.\begin{array}{r}M_0(\mathrm{TP}_2) = M_i/\cos(\chi + \alpha_i)\\[6pt]\beta_i(\mathrm{TP}_2) = \dfrac{\pi}{2} - \alpha_i - \chi\end{array}\right\}, \qquad (4.1a,b)$$

where χ represents the trajectory angle of TP_2, which is defined as the angle with respect to the *x*-axis direction.

Following the three-shock theory, we apply oblique shock relations near TP_2. These relations are used across MS_1 for weak solution, across RS_2 for weak solution normally but only when $M_2(\mathrm{TP}_2) < 1$ for strong solution. Additionally, these relations are applied across MS_2 for strong solution.

The matching conditions across SL_2 separating regions (2) and (3) are

$$\left.\begin{array}{r}p_3/p_0 = p_2/p_0 = (p_2/p_1)(p_1/p_0)\\[6pt]\delta_3(\mathrm{TP}_2) = \delta_1(\mathrm{TP}_2) \pm \delta_2(\mathrm{TP}_2)\end{array}\right\}, \qquad (4.2a,b)$$

where $\delta_3(\mathrm{TP}_2) = \delta_1(\mathrm{TP}_2) - \delta_2(\mathrm{TP}_2)$ for a 'standard' triple-shock configuration and $\delta_3(\mathrm{TP}_2) = \delta_1(\mathrm{TP}_2) + \delta_2(\mathrm{TP}_2)$ for a 'non-standard' triple-shock configuration.

To quantify the triple-shock configuration surrounding TP_2, we measure the shock front parameters defined in figure 9(*a*) from figures 5(*a*) and 5(*b*). The resulting values for MS_1 are $M_i = 1.62$ and $\alpha_i = 14.4°$, while the value for MS_2 is $M_m = 1.83$. Figure 9(*b*) illustrates a shock-polar solution of the incident triple-shock configuration, where positive angles correspond to anticlockwise flow deflections. The numbered regions in figure 9(*a*) correspond to the numbered points of the shock polar intersections. The oncoming flow shock polar is determined by the oncoming flow Mach number $M_0(\mathrm{TP}_2) = 1.94$, originating from the origin. Point (1) lies on the oncoming flow shock polar at $\delta_1(\mathrm{TP}_2) = 20.3°$. The flow parameters immediately behind MS_1 (i.e. region (1)) are utilized to determine the reflection shock polar for region (1), which originates from point (1). The intersection point between the shock polar for region (1) and the oncoming flow shock polar, labelled (2) and (3), represents the theoretical solution for the flow states in regions (2) and (3), respectively. The theoretical pressure ratio of 3.74 in regions (2) and (3) agrees well with the computed value of 3.73. Additionally, the theoretical value of the
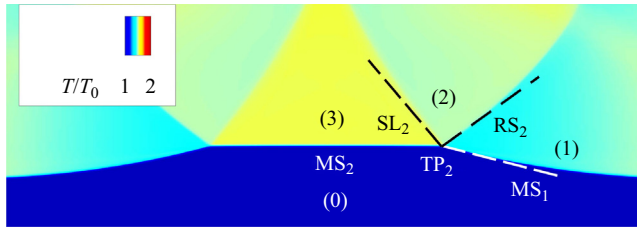
984 A49-14

Figure 10. Comparison between the analytical wave configuration (denoted by dashed lines) and the numerical contour of the normalized temperature.
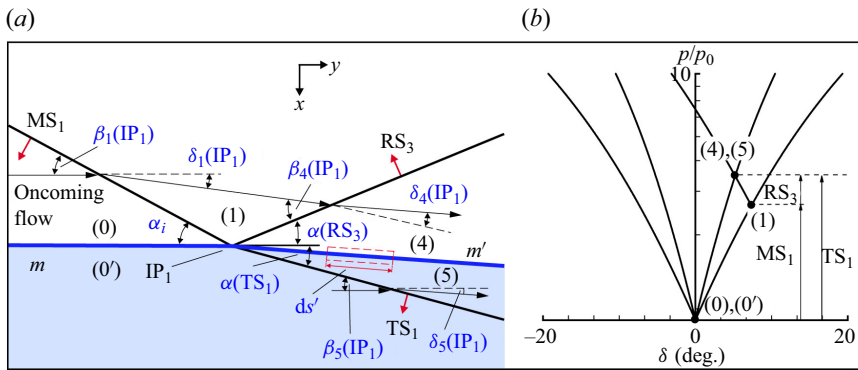

Figure 11. (*a*) Schematic illustration of the primary refraction of MS_1 at the initial interface and (*b*) shock-polar solution of the primary refraction of MS_1 at a N_2–Kr interface. The solid points represent the solution points.

triple point trajectory angle (χ) is approximately $18.9°$, which also agrees satisfactorily with the numerical value ($18.6°$) obtained from linearly fitting the trajectory (as displayed in figure 4*b*) of TP_2. Thus, the shock polars can be used to distinguish between different types of shock reflection and quantify the strength and orientation of RS_2. The reflected shock (RS_2) and the shear layer (SL_2), obtained from the shock polar analysis, are superimposed on the numerical contour of the normalized temperature T/T_0 in figure 10 for comparison, showing a good agreement. Note that this type of shock reflection should be categorized as von Neumann reflection (Ben-Dor 2007; Vasilev *et al.* 2008; Yang, Li & Wu 2013), since the solution of the three-shock theory is 'non-standard' where $\delta_3(TP_2) = \delta_1(TP_2) + \delta_2(TP_2)$. In other words, the oncoming flow in region (0) is deflected in the same direction successively by MS_1 and RS_2.

4.1.2. *Solution of the primary shock refraction*

As previously shown in figures 6(*b*) and 6(*c*), shocks MS_1 and MS_2 intersect with the initial interface successively, resulting in regular shock refractions. Only the relations related to the refraction of MS_1 are derived below, as those associated with the refraction of MS_2 are similar. The appropriate parts of the resulting wave configurations, generated by the refraction of MS_1 (see figures 6*b*), are enlarged and schematically illustrated in figure 11(*a*). The frame of reference is attached to IP_1 where MS_1, RS_3 and TS_1 intersect at the interface, and all the flow properties that are frame of reference dependent are appropriately marked. Here, γ_0 and γ_0' represent the ratios of specific heats in the
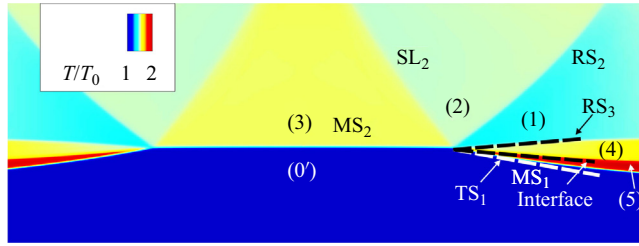
Figure 12. Comparison of wave configurations and interface between analytical prediction (denoted by dashed lines) and numerical result for the primary refraction of MS_1 at a N_2–Kr interface.

incident and transmitted gases, respectively. Here p_0 and $\rho_{0'}$, respectively, denote the initial pressure and density of the flow in region $(0')$.

According to the shock refraction law (Henderson 2014), the incident and transmitted shocks must propagate at the same velocity along the interface. As a result, the parameters of TS_1 can be related to those of MS_1 using the following expression:

$$M(TS_1)a_0'/\sin\alpha(TS_1) = M_i a_0/\sin\alpha_i, \qquad (4.3)$$

where $M(TS_1)$ and $\alpha(TS_1)$ are the Mach number and angle of incidence of TS_1, respectively; $a_0 = \sqrt{\gamma_0 p_0/\rho_0}$ and $a_0' = \sqrt{\gamma_0' p_0/\rho_0'}$ are, respectively, the initial sound speeds of the incident gas in region (0) and the transmitted gas in region $(0')$. In the frame of reference attached to IP_1, the Mach numbers of the oncoming flows in regions (0) and $(0')$ are $M_0(IP_1)$ and $M_{0'}(IP_1)$, respectively, and are derived as

$$\left.\begin{array}{l} M_0(IP_1) = M_i/\sin\alpha_i \\ M_{0'}(IP_1) = M(TS_1)/\sin\alpha(TS_1) = M_i(a_0/a_0')/\sin\alpha_i \end{array}\right\}. \qquad (4.4a,b)$$

The shock angle of MS_1 with respect to the oncoming flow in region (0) is

$$\beta_1(IP_1) = \frac{\pi}{2} - \alpha_i. \qquad (4.5)$$

The oblique shock relations are applied, in the vicinity of IP_1, across MS_1, RS_3 and TS_1. In addition, the matching conditions across the shocked interface m' separating regions (4) and (5) are

$$\left.\begin{array}{l} (p_4/p_1)(p_1/p_0) = p_5/p_0 \\ \delta_1(IP_1) - \delta_4(IP_1) = \delta_5(IP_1) \end{array}\right\}. \qquad (4.6a,b)$$

Figure 11(b) presents the shock-polar solution of the primary refraction of MS_1 for the case of N_2–Kr interface. The shock polars for region (0) and $(0')$ are determined by the oncoming flow conditions $M_0(IP_1) = 6.51$, $\gamma_0 = 1.399$ and $M_{0'}(IP_1) = 10.34$, $\gamma_{0'} = 1.661$, respectively. Point (1) is located on the oncoming shock polar for region (0) at the position of $\delta_1(IP_1) = 7.32°$. With the pressure ratio fixed, the Mach number in region (1), $M_1(IP_1) = 5.37$ is uniquely determined, and the shock polar for region (1) can be drawn originating from point (1). Points (4) and (5) on the shock polar diagram have a pressure ratio of 3.81, which is exactly the same as the numerical value. Therefore, the shock polars can be used to quantify the strength of both the reflected and transmitted shocks (RS_3 and TS_1) as well as their incidence angles. As shown in figure 12, the analytical reflected shock (RS_3), transmitted shock (TS_1) and the shocked interface (m') coincide with the numerical contour of the normalized temperature T/T_0.
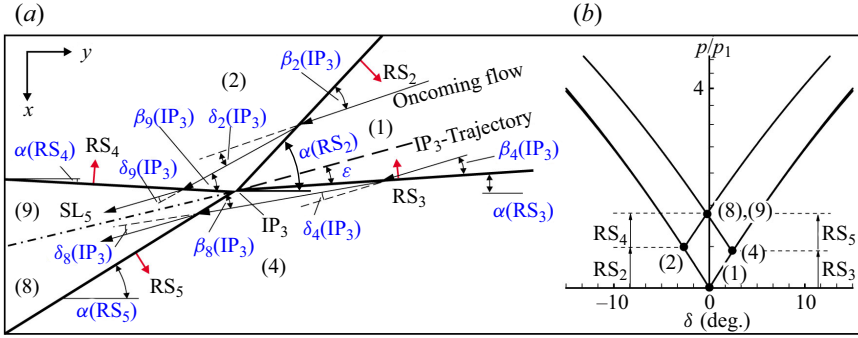
984 A49-16

Figure 13. (*a*) Schematic illustration of the interaction between RS_2 and RS_3 and (*b*) shock-polar solution of the interaction between RS_2 and RS_3 involved in the triple-shock refraction at a N_2–Kr interface. The solid points represent the solution points.

Generally, the velocity of the doubly shocked flow in region (4) is lower than that of the flow in region (5), which has only been shocked by TS_1, resulting in a shear across the interface (Samtaney & Zabusky 1994). Consequently, the refraction process of MS_1 deposits baroclinic vorticity on the interface. By integrating the velocity along a contour with length ds' parallel to the primary shocked interface and infinitesimally thin perpendicular to it, the circulation per unit length (CPUL) of the shocked interface (m') can be obtained as

$$\Gamma'_{m'} = \frac{d\Gamma_{m'}}{ds'} = V_{5t} - V_{4t}, \tag{4.7}$$

where V_{4t} and V_{5t} denote the velocities tangential to m' in the incident gas and the transmitted gas, respectively. Furthermore, (4.7) can be multiplied by the geometric factor $ds'/ds = [\cos \alpha_i / \cos(\alpha_i - \delta_5(IP_1)]$ to yield the CPUL with respect to the initial interface m:

$$\Gamma'_m = \frac{d\Gamma_m}{ds} = (V_{5t} - V_{4t})\frac{\cos \alpha_i}{\cos(\alpha_i - \delta_5(IP_1))}. \tag{4.8}$$

Samtaney & Zabusky (1994) utilized an asymptotic method to provide a first-order estimation of (4.8), and proposed the SZ model, which is formulated as follows:

$$\begin{aligned}\Gamma'_{m,SZ} = \frac{d\Gamma_m}{ds} &= \frac{2\gamma_c^{1/2}}{\gamma_c + 1}(1 - \eta^{-1/2})\sin \alpha_i(1 + M(MS_1)^{-1} \\ &+ 2M(MS_1)^{-2})(M(MS_1) - 1)\sqrt{\frac{p_0}{\rho_0}},\end{aligned} \tag{4.9}$$

where $\gamma_c = (\gamma_0 + \gamma_{0'})/2$ and $\eta = \rho_{0'}/\rho_0$ denote the characteristic specific heat ratio and the density ratio of the preshocked gases across the interface, respectively.

4.1.3. *Solution of the shock–shock interaction*

The flow field surrounding IP_3, where RS_2 and RS_3 interfere, is illustrated in figure 13(*a*). By attaching a frame of reference to IP_3, all the flow properties are appropriately marked. Prior to solving the flow field, the velocity of IP_3 with respect to region (1) should be determined. Considering that the wave configuration around IP_3 retains its structure as it

evolves, i.e. RS_2 and RS_3 proceed at the same velocity with respect to region (1) along the trajectory of IP_3, the following geometric relations hold:

$$|V_{IP_3} - V_1| = \frac{M(RS_2)a_1}{\sin(\alpha(RS_2) - \varepsilon)} = \frac{M(RS_3)a_1}{\sin \varepsilon}, \quad (4.10)$$

where ε is the unknown parameter that represents the trajectory angle of IP_3 with respect to RS_3 (see figure 13a), and the flow parameters $M(RS_2)$, $M(RS_3)$, $\alpha(RS_2)$, V_1 and a_1 are known.

In the frame of reference attached to IP_3, the oncoming flow parameters in region (1) can be expressed as

$$\left.\begin{array}{c} M_1(IP_3) = \dfrac{M(RS_2)}{\sin(\alpha(RS_2) - \varepsilon)} \\ \beta_2(IP_3) = \alpha(RS_2) - \varepsilon \\ \beta_4(IP_3) = \varepsilon \end{array}\right\}. \quad (4.11a\text{–}c)$$

The oblique shock relations are applied, in the vicinity of IP_3, across RS_2, RS_3, RS_4 and RS_5, respectively. In addition, the matching conditions across SL_5 separating regions (8) and (9) are as follows:

$$\left.\begin{array}{c} (p_9/p_2)(p_2/p_1) = (p_8/p_4)(p_4/p_1) \\ \delta_2(IP_3) - \delta_9(IP_3) = \delta_8(IP_3) - \delta_4(IP_3) \end{array}\right\}. \quad (4.12a,b)$$

The shock polars depicted in figure 13(b) illustrate the interaction between RS_2 and RS_3 for the N_2–Kr interface case. State (1) at which $p/p_1 = 1$, $\delta_1(IP_3) = 0$, is located at the origin. The oncoming flow shock polar for region (1) is determined by the oncoming flow Mach number $M_1(IP_3) = 4.20$. The points (2) and (4) are located on the oncoming flow shock polar at the locations of $\delta_2(IP_3) = -2.69°$ and $\delta_4(IP_3) = 2.43°$, respectively. With the pressure ratios $p_2/p_1 = 1.32$ and $p_4/p_1 = 1.29$ fixed, the Mach numbers in regions (2) and (4), $M_2(IP_3) = 3.98$ and $M_4(IP_3) = 4.00$ can be uniquely determined. Consequently, the shock polars for regions (2) and (4) can be drawn originating from point (2) and (4) correspondingly. Points (8) and (9) should coincide at the intersection of shock polars for regions (2) and (4). Note that points (8) and (9) on the shock polar diagram have a pressure ratio of 1.67, which agrees well with the calculated value of 1.63.

4.1.4. *Solution of the secondary shock refraction*

As previously mentioned, RS_5 intersects and interacts with m' at IP_4. This intersection leads to a secondary shock refraction and deposits additional baroclinic vorticity on the interface. The resulting wave configuration from the secondary shock refraction is illustrated in figure 14(a), with the frame of reference being attached to IP_4, and all the flow properties, which are frame of reference dependent are appropriately marked. It should be noted that m' is evolving and not vorticity-free. This differs from the aforementioned primary refractions of MS_1 and MS_2, where the interface m is initially stationary and vorticity-free.

In the frame of reference attached to IP_4, the flow parameters in zones (4) and (5) can be expressed as

$$\left.\begin{array}{c} M_4(IP_4) = M(RS_5)/\sin(\alpha(RS_5) + \delta_4(IP_1)) \\ M_5(IP_4) = M_4(IP_4)(a_4/a_5) \\ \beta_8(IP_4) = \alpha(RS_5) + \delta_4(IP_1) \end{array}\right\}, \quad (4.13a\text{–}c)$$

where $M(RS_5)$, $\alpha(RS_5)$, $\delta_4(IP_1)$, a_4 and a_5 are known.
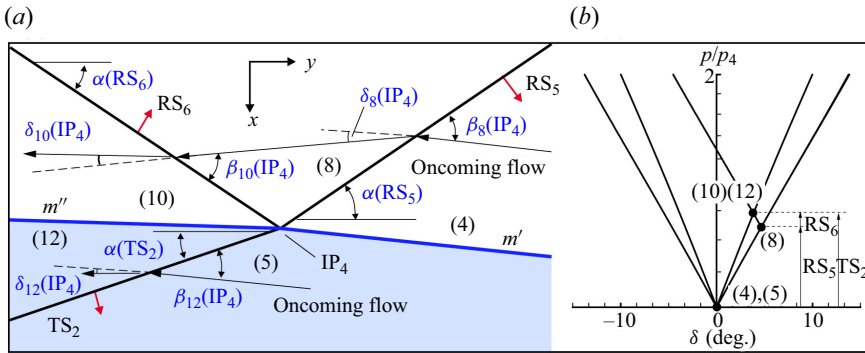
Figure 14. (*a*) Schematic illustration of the secondary refraction of RS_5 and (*b*) shock-polar solution of the secondary refraction of RS_5 involved in the triple-shock refraction at a N_2–Kr interface. The solid points represent the solution points.

The oblique shock relations are applied, in the vicinity of IP_4, across RS_5, RS_6 and TS_2, respectively. In addition, the matching conditions across the secondary shocked interface (m'') separating regions (10) and (12) are

$$(p_8/p_4)(p_{10}/p_8) = p_{12}/p_5 \atop \delta_8(IP_4) - \delta_{10}(IP_4) = \delta_{12}(IP_4) \Bigg\}. \qquad (4.14a,b)$$

Figure 14(*b*) illustrates the shock-polar solution of the secondary shock refraction of RS_5 for the case of the N_2–Kr interface. The oncoming flow shock polars for regions (4) and (5) are determined by $M_4(IP_4) = 1.76$, $\gamma_0 = 1.399$ and $M_5(IP_4) = 2.33$, $\gamma_{0'} = 1.661$, respectively. Point (8) is located on the shock polar for region (4) at $\delta_8(IP_4) = 4.67°$. With the location of point (8) now fixed, the Mach number in region (8), $M_8(IP_4) = 1.60$, can be uniquely determined, allowing for drawing a shock polar originating from point (8). Note that point (12) must lie on the $M_5(IP_4) = 2.33$, $\gamma_{0'} = 1.661$ shock polar, and point (10) must coincide with point (12) because regions (10) and (12) are separated by the interface m''. Consequently, points (10) and (12) lie on the intersection of the shock polars for regions (5) and (8). In this case, the analytical postshock pressure ratio $p_{10}/p_4 = 1.32$ agrees with the numerical value of 1.33. Therefore, the shock polars provide a quantitative assessment of both the strength and orientation of the transmitted shock TS_2 and the reflected shock RS_6.

The secondary refraction of RS_5 alters the tangential velocities across the secondary shocked interface m'' and generates secondary baroclinic vorticity along the interface. By considering the jump in tangential velocity across m'' and incorporating the geometric factor $ds''/ds = [\cos \alpha_i / \cos(\alpha_i - \delta_5(IP_1))][\cos(\alpha(RS_5) + \delta_5(IP_1))/\cos(\alpha(RS_5) + \delta_5(IP_1) - \delta_{12}(IP_4))]$, the CPUL with respect to the initial interface m is derived as

$$\Gamma_m' = \frac{d\Gamma_m}{ds} = (V_{12t} - V_{10t}) \frac{\cos(\alpha(RS_5) + \delta_5(IP_1))}{\cos(\alpha(RS_5) + \delta_5(IP_1) - \delta_{12}(IP_4))} \frac{\cos \alpha_i}{\cos(\alpha_i - \delta_5(IP_1))}. \qquad (4.15)$$

4.2. *Analytical solution of the transmitted wave configuration*

As mentioned earlier, depending on Z_r, an incident triple-shock configuration can be transmitted as either a triple-shock configuration, a four-wave configuration or a four-shock configuration. In this section, the relevant parts of the transmitted wave configurations

around TP$_3$, depicted in figures 6(*d*) and 8, are enlarged and schematically illustrated in figure 15(*a*i,*b*i,*c*i). The transmitted wave configuration can be interpreted as the reflection of TS$_1$ at the symmetry axis. In addition, TS$_1$, TS$_2$ and MS$_3$ serve as the incident shock, reflected shock and Mach stem, respectively, for a general triple-shock configuration. Hence, a similar methodology employed in the analysis of the incident triple-shock configuration (see § 4.1.1) can be applied to investigate the transmitted wave configuration.

In the frame of reference attached to TP$_3$, the oncoming flow parameters in region (0') can be derived as

$$\left.\begin{array}{c} M_{0'}(\text{TP}_3) = M(\text{TS}_1)/\cos(\chi_1 + \alpha(\text{TS}_1)) \\ \beta_5(\text{TP}_3) = \dfrac{\pi}{2} - \alpha(\text{TS}_1) - \chi_1 \end{array}\right\}, \tag{4.16a,b}$$

where χ_1 represents the trajectory angle of TP$_3$ with respect to the *x*-axis direction.

4.2.1. *Solution of the transmitted triple-shock configuration*

For the transmitted triple-shock configuration depicted in figure 15(*a*), the oblique shock relations are applied across TS$_3$, MS$_3$ and TS$_2$. In addition, the match conditions across SL$_3$ are written as

$$\left.\begin{array}{c} (p_{12}/p_5)(p_5/p_{0'}) = p_7/p_{0'} \\ \delta_5(\text{TP}_3) \pm \delta_{12}(\text{TP}_3) = \delta_7(\text{TP}_3) \end{array}\right\}. \tag{4.17a,b}$$

The shock-polar solution of the triple-shock configuration transmitted into air is shown in figure 15(*a*ii,*b*ii,*c*ii). The region (0') is represented by the origin, where $p = p_{0'}$ and $\delta_{0'}(\text{TP}_3) = 0$. Point (5) lies on the $M_{0'}(\text{TP}_3) = 1.94$, $\gamma_{0'} = 1.399$ oncoming flow shock polar at the location $\delta_5 = 20.45°$. With the pressure ratio $p_5 = 2.92$ fixed, the Mach number in region (5) is determined to be $M_5(\text{TP}_3) = 1.12$, and the shock polar for region (5) can be drawn originating from point (5). Here SL$_3$ separates the flow in region (12) which has been compressed successively by both TS$_1$ and TS$_2$ from the flow in region (7) that has only compressed by MS$_3$. Therefore, points (7) and (12) lie on the intersection of the shock polar originating from point (5) and the oncoming flow shock polar. Points (7) and (12) on the shock polar diagram share a pressure ratio of 3.75, which agrees with the numerical value of 3.76. It is noteworthy that the transmitted triple-shock configuration can also be identified as a von Neumann reflection of TS$_1$ at the symmetry axis, since (4.16*a,b*) and (4.17*a,b*) provide a 'non-standard' solution for the three-shock theory, i.e. $\delta_7(\text{TP}_3) = \delta_5(\text{TP}_3) + \delta_{12}(\text{TP}_3)$.

4.2.2. *Solution of the transmitted four-shock configuration*

For the transmitted four-shock configuration depicted in figure 15(*b*), the match conditions across the SL$_3$ are written as

$$\left.\begin{array}{c} (p_{13}/p_{12})(p_{12}/p_5)(p_5/p_{0'}) = p_7/p_{0'} \\ \delta_5(\text{TP}_3) \pm \delta_{12}(\text{TP}_3) \pm \delta_{13}(\text{TP}_3) = \delta_7(\text{TP}_3) \end{array}\right\}. \tag{4.18a,b}$$

In addition to the equations governing the transmitted triple-shock configuration, it is necessary to supplement the shock relations across TS$_3$. Besides, considering that the leading shock front of the incident triple-shock configuration has just passed through the interface and the length of TS$_2$ is limited, it is reasonable to assume that TS$_2$ is straight. The shock angle $\beta_{12}(\text{TP}_3)$ can subsequently be derived as

$$\beta_{12}(\text{TP}_3) = \alpha(\text{TS}_2) + \left(\dfrac{\pi}{2} - \chi_1 - \delta_5(\text{TP}_3)\right), \tag{4.19}$$

where $\alpha(\text{TS}_2)$ denotes the angle of TS$_2$ with respect to the *x*-axis direction.
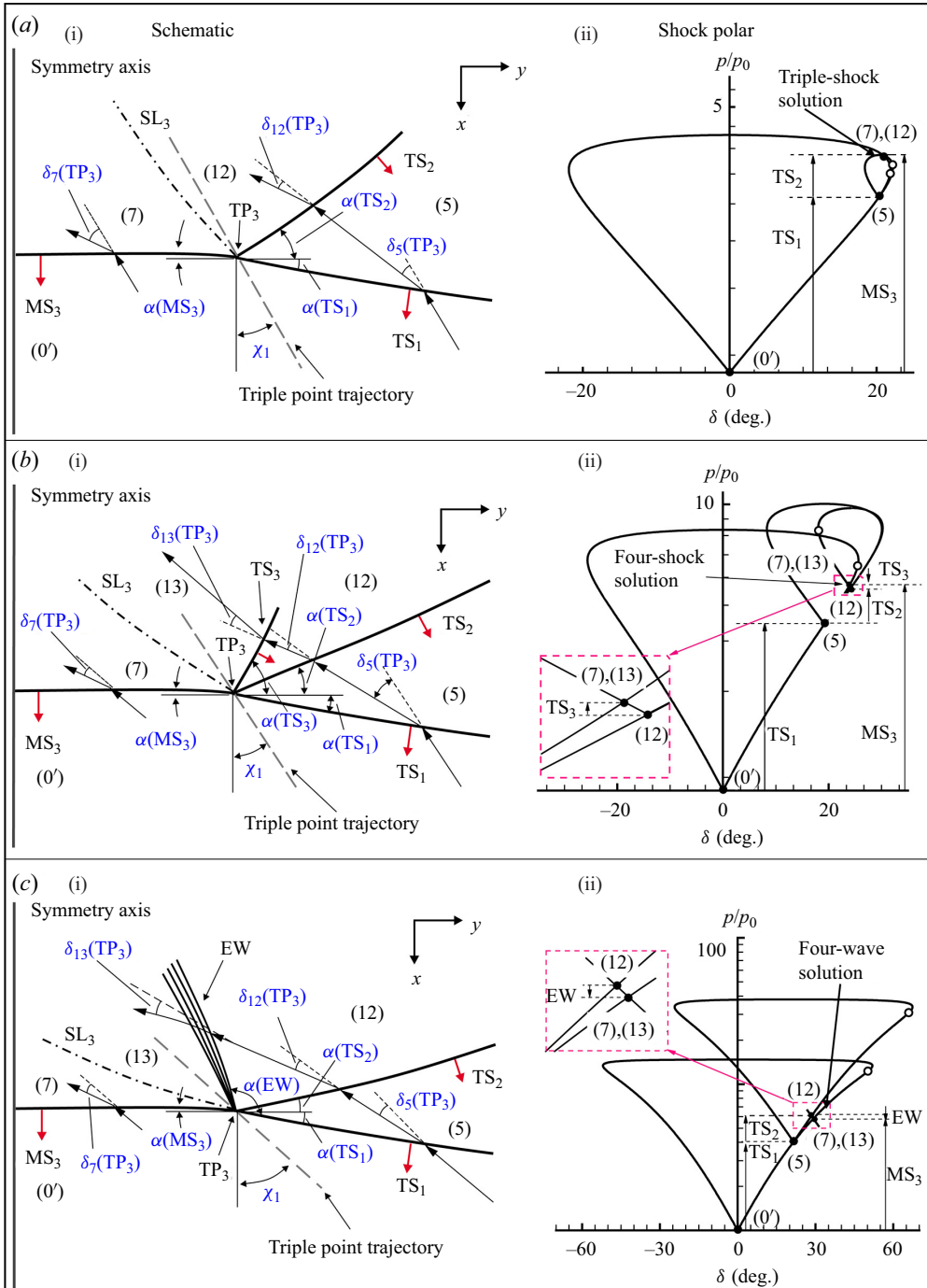
984 A49-20

Figure 15. Schematics of the transmitted wave configurations and their corresponding shock polar representations: (*a*) triple-shock configuration; (*b*) four-shock configuration; (*c*) four-wave configuration. The solid points represent the solution points, and the hollow circles denote the sonic points.

Figure 15(b) illustrates the shock-polar solution of the transmitted four-shock configuration, which is drawn precisely by solving the flow properties resulting from the triple-shock refraction at a N_2–Kr interface. region ($0'$) is represented by the origin, where $p = p_{0'}$ and $\delta_{0'}(\mathrm{TP}_3) = 0$. The oncoming flow shock polar is determined by $M_{0'}(\mathrm{TP}_3) = 2.59$, $\gamma_{0'} = 1.661$. Points (5) lies on the oncoming flow shock polar at the locations $\delta_5(\mathrm{TP}_3) = 21.56°$. With the pressure ratio $p_5/p_{0'} = 3.82$ fixed, the flow Mach number in region (5) is determined to be 1.52, and the shock polar for region (5) can be drawn originating from point (5). The shock polar for region (5) intersects with the subsonic branch of the oncoming flow shock polar, thereby yielding a standard solution of the three-shock theory. However, the non-physical nature of this triple-shock solution arises from the fact that the pressure ratio p_7/p_0, determined by the primary refraction of MS_2, suggests that point (7) should lie on the supersonic branch of the oncoming flow shock polar. As a result, a reflection involving a triple-shock solution is unfeasible. Instead, a four-shock theory should be employed here, taking into account the fourth shock wave that emanates between the shock TS_2 and the slipstream SL_3. Considering that the pressures are equal and the flow streams are parallel in regions (7) and (13), it follows that points (7) and (13) must coincide at the intersection of the oncoming flow shock polar and the shock polar for region (12). Therefore, point (12) and its corresponding shock polar can be determined by originating from a specific point on the shock polar for region (5). Points (7) and (13) on the shock polar diagram share a pressure ratio of 5.18, which agrees the numerical value of 5.15.

4.2.3. *Solution of the transmitted four-wave configuration*

For the transmitted four-wave configuration shown in figure 15(c), the match conditions across SL_3 are written as

$$\left.\begin{array}{l}(p_{13}/p_{12})(p_{12}/p_5)(p_5/p_{0'}) = p_7/p_0 \\ \delta_5(\mathrm{TP}_3) + \delta_{12}(\mathrm{TP}_3) + \delta_{13}(\mathrm{TP}_3) = \delta_7(\mathrm{TP}_3)\end{array}\right\}. \qquad (4.20a,b)$$

In addition to the relations governing the transmitted triple-shock configuration, it is necessary to supplement the Prandtl–Meyer conservation relations across EW.

The shock-polar solution of the four-wave configuration transmitted into SF_6 is depicted in figure 15(c). Point (5) is on the $M_{0'}(\mathrm{TP}_3) = 3.76$, $\gamma_{0'} = 1.094$ oncoming flow shock polar at the location $\delta_5(\mathrm{TP}_3) = 21.56°$. The region (5) shock polar intersects the subsonic branch of the oncoming flow shock polar at two points, providing two triple-shock solutions. However, these two solution points are both non-physical, since the pressure ratio p_7/p_0, determined by the primary refraction of MS_2, suggests that point (7) should lie on the supersonic branch of the oncoming flow shock polar. regions (13) and (12) are connected by a weak Prandtl–Meyer expansion fan since the flow in region (12) is slightly underexpanded with respect to the flow in region (7). The solution points (7) and (13) lie on the intersection of the isentropic expansion path originating from point (12) and the oncoming flow shock polar. Points (7) and (13) on the shock polar diagram share a pressure ratio of 5.41, which agrees reasonably well with the value of 5.35 from numerical simulation. Note that points (7) and (13) are located on the supersonic branch of the oncoming flow shock polar, while point (12) lies on the supersonic branch of the shock polar for region (5). The shock-polar solution reveals that the flow regions (7), (12) and (13) are supersonic in the frame of reference attached to TP_3, indicating that this four-wave configuration is distinct from both the Vasilev reflection characterized by two subsonic regions near the triple point and the Guderley reflection featuring one subsonic region near the triple point (Vasilev *et al.* 2008).

4.3. *Application and validation of the analytical model*

In §§ 4.1 and 4.2, the triple-shock refraction process is divided into five subprocesses, and the flow fields associated with these subprocesses are solved separately, and their corresponding analytical models are developed. In this subsection, the entire set of analytical model equations will be solved in combination to determine the wave angles and the flow properties. These analytical results are validated against the numerical simulations. By utilizing the flow properties derived from the analytical model, we aim to quantitatively assess the contributions of triple-shock refraction to the evolution of interface. Furthermore, a shock-polar analysis is carried out for each of the three transmitted wave configurations to gain physical insights into the mechanisms that determine the pattern of the transmitted wave.

4.3.1. *Analytical quantification of the circulation deposition and velocity perturbation*
The morphology of the interface immediately after the triple-shock refraction, as illustrated in figure 16(*a*), can be divided into three distinct segments labelled as I, II and III. The central segment I, which represents the interface accelerated by MS_2, exhibits relative isolation due to its enclosure within SL_3. The outer segment II is characterized by the acceleration of MS_1, and it is matched with the central segment I by an inner segment III that undergoes successive accelerations of both MS_1 and RS_5. Note that the outward propagation of RS_5 will lead to a rapid increase in the length of the segment III, while the segment II will undergo significant shrinkage. As noted in our pervious works (Zou *et al.* 2017; Liao *et al.* 2019), the velocity difference between segments I and III serves as the velocity perturbation, which is responsible for the formation of the central interface cavity. Therefore, it is imperative to conduct a comprehensive theoretical assessment of this velocity perturbation. In addition to the velocity perturbation, baroclinic vorticity typically acts as another governing factor influencing interface evolution. However, Zou *et al.* (2017, 2019) stated that vorticity deposited on the interface is limited due to the small incidence angle of the leading shock front. Liao *et al.* (2019) also reported that the influence of baroclinic circulation becomes prominent only in cases with high incident shock Mach numbers. Qualitative analysis in § 3.2.1 suggests that the relatively insignificant contribution of baroclinic circulation may be attributed to the secondary refraction of RS_5, which partially suppresses the baroclinic vorticity on the interface. The present subsection aims to quantitatively assess the relative contribution of the secondary refraction to the vorticity deposition.

Note that the incident triple-shock configuration is unsteady, and its strength and incidence angle vary continuously during the triple-shock refraction, significantly complicating the calculation of the velocity perturbation and circulation deposition. However, since the triple-shock refraction occurs over an extremely short period, the shock Mach number and the incidence angle involved are assumed to be invariant. Besides, considering the limited length of segment III immediately following the triple-shock refraction, it is reasonable to assume a uniform flow field along this particular segment. Under these two assumptions, the flow fields across the segments I, II and III can be solved theoretically. The input data for the theoretical analysis consists of shock front parameters, including the shock Mach number and incidence angle (as depicted in figure 5), along with the state parameters of gases on both sides of the interface. The initial solution involves solving the primary refractions of MS_1 and MS_2 at the initial interface for segments I and II, respectively, followed by addressing the secondary refraction of RS_5 for segment III.

The triple-shock refraction at a N_2–Kr interface is selected to demonstrate the shock-polar solution of the successive refractions of MS_1 and RS_5, as depicted in
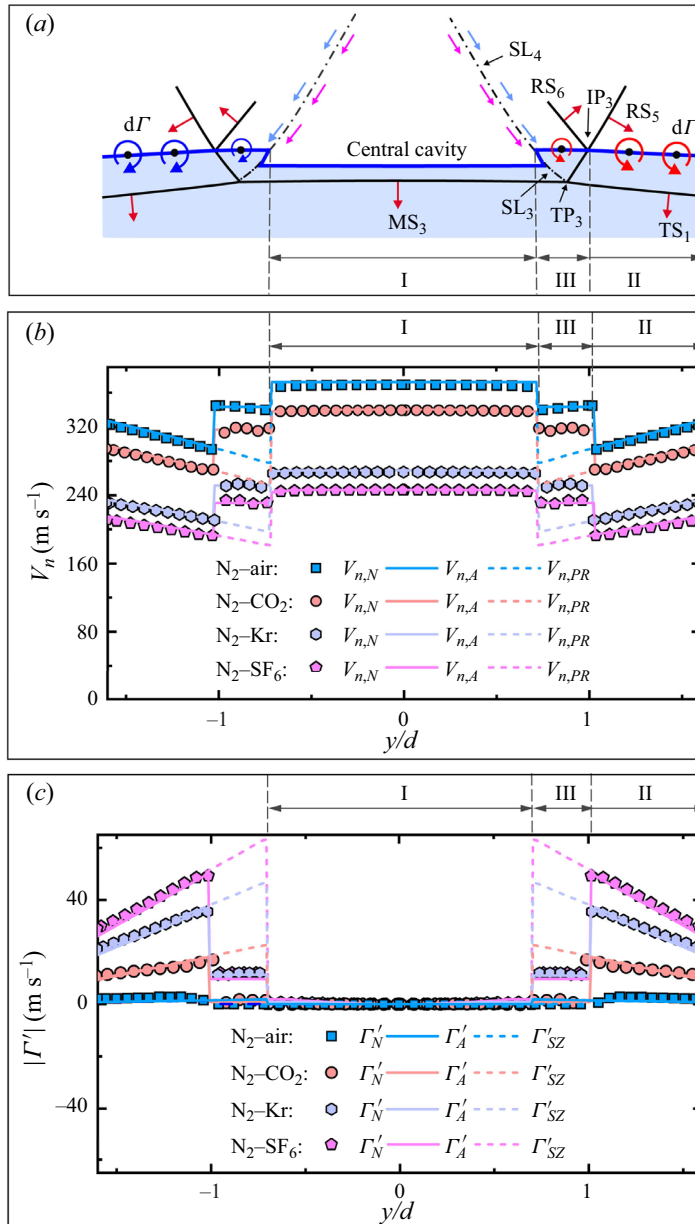
Figure 16. Schematic diagram of the morphology of the interface immediately after triple-shock refraction (*a*) and the imparted longitudinal velocity (*b*) and deposited circulation along the interface (*c*). Here, $V_{n,N}$, $V_{n,A}$ and $V_{n,PR}$ represent the longitudinal velocity of the interface calculated through numerical simulations, predicted by the analytical model, and obtained from theoretical evaluation results that only consider the primary refraction of the leading shock front, respectively. Here Γ'_N, Γ'_A and Γ'_{SZ} denote the CUPL obtained from numerical simulations, analytical model predictions and SZ model predictions, respectively.

figure 17. This figure presents an appropriate combination of the shock polars depicted in figures 9(*b*), 11(*b*), 13(*b*) and 14(*b*). Correspondingly, the shock polars can be classified into four groups, denoted as ①, ②, ③ and ④, respectively. The shock polars of group ① represent the solution of the regular refraction of MS_1 at the initial interface. This solution
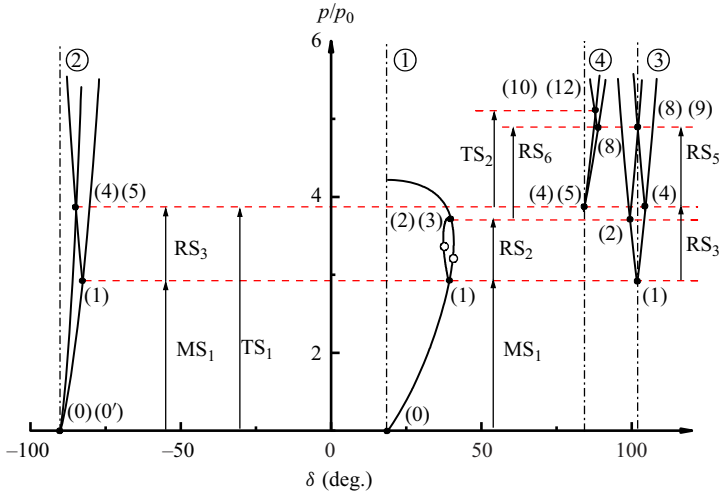
Figure 17. Shock polars illustrating the successive refractions of MS_1 and RS_5 at a N_2–Kr interface. The solid points represent the solution points, and the hollow circles denote the sonic points.

is derived from a frame of reference attached to IP_1, with the origin labelled as (0) and $(0')$ at $\delta = -90°$, $p = p_0$. The shock polars of group ② correspond to the characterization of the incident triple-shock configuration. Since the incident triple-shock configuration is solved from a frame of reference attached to TP_1, the origin of the shock polars of group ② (labelled as (0)) is located at $\delta = \chi$, $p = p_0$. The shock polars of group ③ represent the solution of the shock–shock interaction between RS_2 and RS_3. This solution is derived from a frame of reference attached to IP_3, with its origin labelled as (1) located at $\delta = 90° + \chi_2$, $p = p_1$. It should be noted that the pressures in regions (2) and (4) remain unchanged regardless of the chosen frame of reference. It is also noticed that points (2) and (4) on the shock polars of group ③ are determined by solutions obtained from shock polars of groups ① and ②. Therefore, points (2) and (4) of group ③ are bridged with the corresponding points on shock polars of groups ① and ② through the constant p_2 line and constant p_4 line, respectively, as indicated by horizontal red dashed lines in figure 17. The shock-polar solution of the secondary refraction of RS_5 is illustrated by the shock polars of group ④. Points (4) and (5) serve as the origin of shock polars of group ④, which represents the flow states on both sides of m', and are bridged with points (4) and (5) on the shock polars of group ① by the constant p_4 line. Point (8) on shock polars of group ④ represents the flow state behind the shock RS_5 in the incident gas and is bridged with point (8) on shock polars of group ③ by the constant p_8 line. Finally, the determination of flow states (10) and (12) on both sides of m'', relies on identifying the intersection point between shock polars for regions (8) and (5) within group ④.

Once the flow properties of regions across the postshock interface (i.e. regions (4), (5), (6), (7), (10) and (12) in figure 6d) are determined, the CPUL deposited on the interface can be evaluated using (4.8) and (4.15). Regarding the evaluation of the velocity perturbation, the longitudinal velocities of the gases differ across an inclined interface. Therefore, V_n is employed to denote the longitudinal velocity of the interface, which is calculated by $V_n = (u_{light} + u_{heavy})/2$ with u_{light} (u_{heavy}) representing the velocity of the light (heavy) gas in the x-axis direction in close proximity to the interface. Additionally, $V_p = (V_{n,\mathrm{I}} - V_{n,\mathrm{III}})$ defines the velocity perturbation of the interface, where $V_{n,\mathrm{I}}$ and $V_{n,\mathrm{III}}$ correspond to characteristic longitudinal velocities of the segments I and III. In this

Gas combination	$V_{p,N}$ (m s^{-1})	$V_{p,A}$ (m s^{-1})	$V_{p,PR}$ (m s^{-1})	$\mathcal{R}_{V,SR}$ (%)	$\Gamma'_{III,N}$ (m s^{-1})	$\Gamma'_{III,A}$ (m s^{-1})	$\Gamma'_{III,SZ}$ (m s^{-1})	$\mathcal{R}_{\Gamma',SR}$ (%)
N$_2$–air	28.6	28.9	94.4	−69.4	0.2	0.1	1.9	−94.7
N$_2$–CO$_2$	23.9	23.5	88.3	−73.4	1.1	0.7	22.6	−96.0
N$_2$–Kr	18.1	17.8	71.1	−70.8	11.9	11	46.6	−76.4
N$_2$–SF$_6$	15.1	15.5	65.3	−76.3	12.1	10.2	63.2	−83.8

Table 2. The velocity perturbation and CPUL of the interface resulting from the triple-shock refraction at four distinct interfaces. Here, $V_{p,N}$, $V_{p,A}$, and $V_{p,PR}$ represent the velocity perturbations of the interface calculated through numerical simulations, predicted by the analytical model, and obtained from theoretical evaluations that only consider the primary refraction of the leading shock front, respectively. Here $\Gamma'_{III,N}$, $\Gamma'_{III,A}$ and $\Gamma'_{III,SZ}$ denote the CPUL of the interface obtained from numerical simulations, analytical model predictions and SZ model predictions, respectively. Here $\mathcal{R}_{V,SR}$ and $\mathcal{R}_{\Gamma',SR}$ (%), respectively, represent the relative contributions of the secondary shock refraction of RS$_5$ to the velocity perturbation and circulation deposition.

context, the characteristic velocity for the segment I is determined as the longitudinal velocity of the centre of segment I, while for the segment III, it is determined by the longitudinal velocity of the segment III near its intersection with the segment I.

The longitudinal velocity distribution resulting from the triple-shock refraction at four distinct interfaces is analytically evaluated and validated against the numerical results, as illustrated in figure 16(*b*). Additionally, to highlight the contribution of the secondary refraction of RS$_5$, theoretical evaluations considering only the primary refraction of the leading shock front (i.e. MS$_1$ and MS$_2$) are also presented for comparison. Overall, the analytical results agree well with numerical counterparts across a wide range of initial conditions. The results show that the longitudinal velocity of the interface increases monotonically from IP$_3$ along the segment II due to the enhancement of MS$_1$. Notably, the segment I exhibits a greater longitudinal velocity compared with both the segments II and III due to the relatively stronger MS$_2$, validating the qualitative analysis in § 3.2.1. Another remarkable feature is that the segment III acquires a substantial longitudinal velocity through the secondary shock refraction, effectively inhibiting the velocity perturbation of the interface. The velocity perturbations are computed and presented in table 2, and a good agreement between the analytically and numerical values is reached. Note that the velocity perturbations of the interface exhibit a monotonic decrease as Z_r increases. This observation provides an explanation for the decrease in growth rate of interface perturbation amplitude with increasing Atwood number, as reported by Liao *et al.* (2019). To quantitatively assess the relative contribution of the secondary shock refraction to the velocity perturbation, we define $\mathcal{R}_V(= (V_{p,A} - V_{p,PR})/V_{p,PR} \times 100\%)$ as the ratio between the velocity perturbation inhibited by the secondary shock refraction and that induced by the primary shock refraction. As demonstrated in table 2, the velocity perturbation of the interface is significantly influenced by the secondary shock refraction (i.e. the value of $|\mathcal{R}_{V,SR}|$ is greater than 69.4 % for all the cases). Therefore, when estimating the velocity perturbation of the interface induced by a non-uniform shock with inherent triple-shock configurations, the contribution of reflected shocks travelling behind the leading shock front cannot be ignored.

The CPUL of the four distinct interfaces resulting from the triple-shock refraction is analytically evaluated and compared with both the numerical results and the predictions of the SZ model. As illustrated in figure 16(*c*), the analytical results exhibit satisfactory agreement with those obtained from numerical simulations. However, the SZ model overpredicts the CPUL of the segment III, because it does not consider the secondary

refraction of RS_5. The CPUL of the segment II displays a positive correlation with the increase in Z_r, which can be attributed to the corresponding rise in density gradient across the interface. It is noteworthy that upon encountering the interface, MS_3 refracts nearly perpendicularly, generating limited vorticity on the segment I. Besides, the CPUL of the segment II exhibits a monotonic decrease from IP_3, primarily attributed to the reduction in incidence angle of MS_1 along this segment. The CPUL of the segment III is extracted from figure 16(*c*) and presented in table 2. To quantitatively evaluate the relative contribution of the secondary shock refraction to the vorticity deposition, we define $\mathcal{R}_{\Gamma',SR}(= (\Gamma'_{\text{III},A} - \Gamma'_{\text{III},SZ})/\Gamma'_{\text{III},SZ} \times 100\%)$ as the ratio between the CPUL suppressed by the secondary shock refraction and that deposited by the primary shock refraction. As demonstrated in table 2, the secondary shock refraction significantly contributes to the circulation of the interface (i.e. the value of $|\mathcal{R}_{\Gamma',SR}|$ is greater than 76.4% for all the cases). This observation sheds light on the underlying mechanism of a puzzling phenomenon, namely the relatively insignificant contribution of vorticity to the RM-like instability (Liang *et al.* 2017; Zou *et al.* 2017; Liao *et al.* 2019; Zou *et al.* 2019).

4.3.2. *Analytical prediction of the transmitted wave configuration*

The shock polar solution of the transmission of the incident triple-shock configuration at a N_2–air interface is shown in figure 18(*a*), with numbered regions corresponding to figure 6(*d*). The shock polars can be categorized into three groups, denoted as ①, ② and ③, respectively. The shock polars of group ① represent the solution of the refraction of MS_2 at the initial interface, while those of group ② depict the solution of the refraction of MS_1. The solutions for these two primary shock refractions are derived from frames of reference attached to their corresponding shock–interface intersection points, which move in the negative *y*-axis direction. Therefore, the origins of the shock polars of group ① and ② labelled as (0) and (0′), respectively, are located at $\delta = -90°$, $p = p_0$. The shock polars of group ③ represent the solution of the transmitted triple-shock configuration, which is derived from a frame of reference attached to TP_3. Therefore, the origin of the shock polars of group ③ is located at $\delta = \chi_1$, $p = p_0$. Note that the shock polars of groups ① and ② are solved in frames of reference with higher velocities compared with that of group ③. Consequently, the shock polars for region (0′) in groups ① and ② are larger than that for region (0′) of group ③. The pressures in zones (5) and (7) remain unchanged regardless of the chosen frame of reference. Therefore, the shock polar for region (0′) of group ① is bridged with that of group ③ through the constant p_7 line. Similarly, the shock polar for region (0′) of group ② is bridged with that of group ③ through the constant p_5 line. These two bridge lines are shown as horizontal red dashed lines in figure 18(*a*). It is evident that the shock polars for region (5) and (0′) of group ③ intersect at their subsonic branches, resulting in a non-standard triple-shock solution. Therefore, the flows of regions (7) and (12) are subsonic in the vicinity of TP_3.

In general, the shock polar solution of the transmission of the incident triple-shock configuration at a N_2–Kr interface exhibits similar characteristics to that for the case of a N_2–air interface, with discrepancies observed only in the shock polars of group ③. As illustrated in figure 18(*b*), point (7) is located on the supersonic branch of the shock polar for region (0′) of group ③, while the shock polar for region (5) lies below that for region (0′). There is no intersection between the shock polars for regions (5) and (0′) of group ③, indicating the absence of a triple-shock solution. Instead, a four-shock solution is obtained, where the shock polar originating from point (12) bridges a supersonic state on the shock polar for regions (0′) at point (7) with another supersonic state on the shock polar for region (5). Consequently, both flows in regions (7), (12) and (13) are found
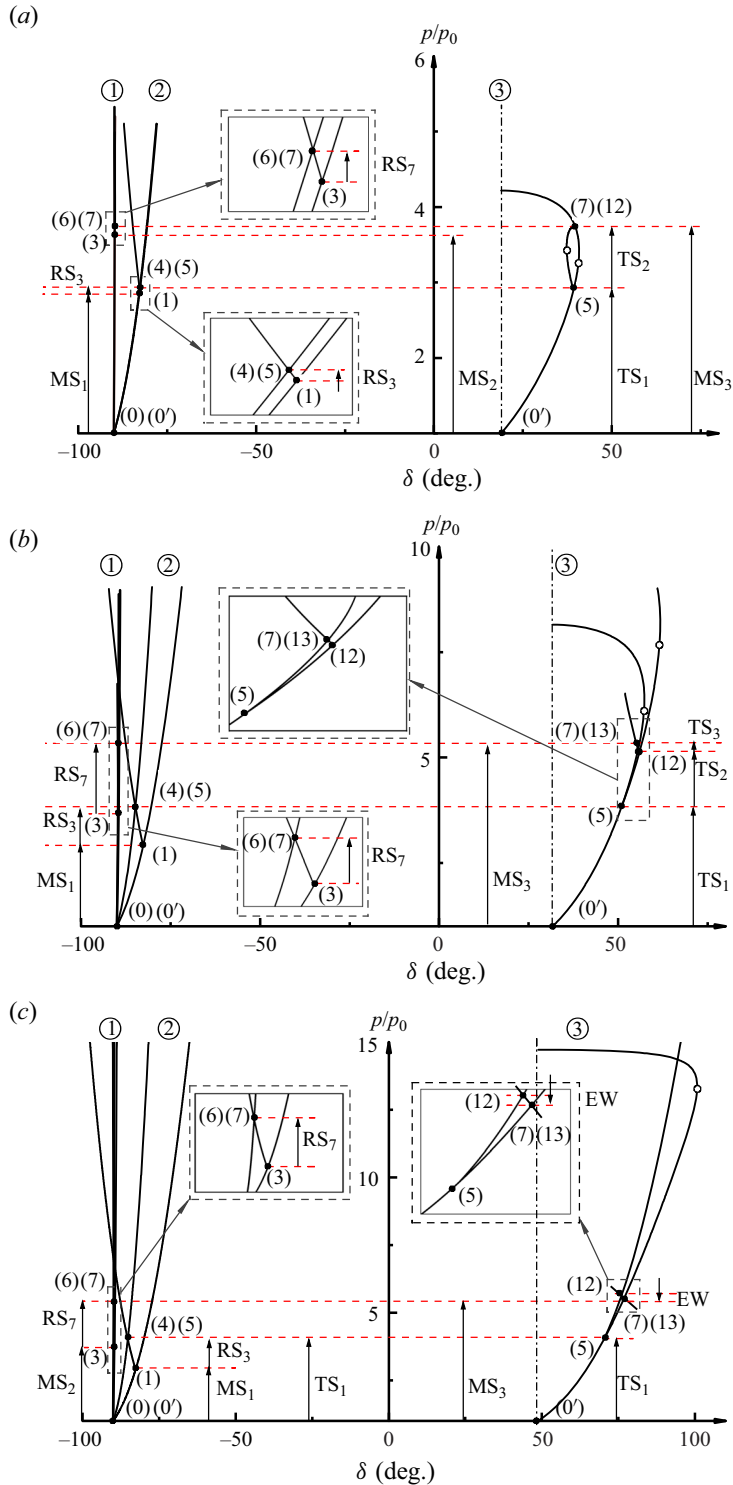
Figure 18. Shock-polar solution of the transmission of the incident triple-shock configuration at (*a*) a N_2–air interface, (*b*) a N_2–Kr interface and (*c*) a N_2–SF$_6$ interface. The solid points represent the solution points, and the hollow circles denote the sonic points.
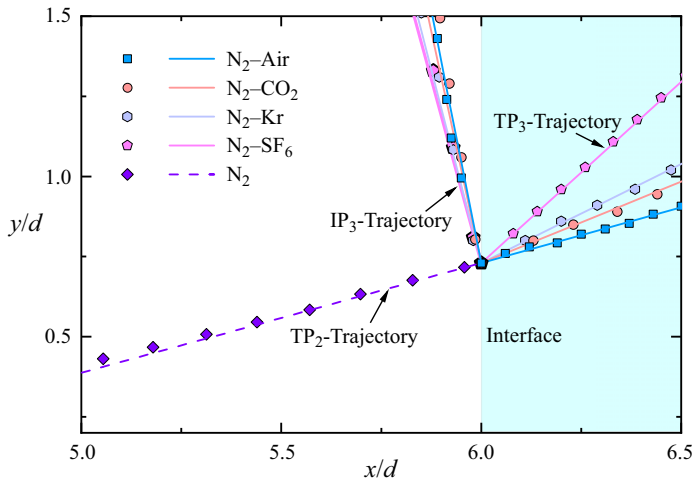
Figure 19. Comparison of trajectories of TP_2, TP_3 and IP_3 between analytical (lines) and numerical (symbols) results.

to be supersonic near TP_3. The transmitted four-shock configuration, obtained through numerical simulations and experiments, is illustrated in figure 7. A weak shock TS_2 bridges the flows in regions (12) and (13) whose conditions are sufficient to support a shock.

The shock polar diagram for the case of a N_2–SF_6 interface is presented in figure 18(*c*). Point (7) remains on the supersonic branch of the shock polar for region $(0')$ of group ③, but the shock polar for region (5) is now positioned above the shock polar for region $(0')$, indicating the absence of a triple-shock solution. The shock-polar combinations shown in group ③ of figure 18(*c*) are obtained from an alternative four-wave solution. In this solution, an isentropic expansion path originates from point (12) on the shock polar for region (5) and intersects with the shock polar for regions $(0')$ below its sonic point. Therefore, in the frame of reference attached to TP_3, the flows of regions (7), (12) and (13) are both supersonic near TP_3. The numerically obtained four-wave configuration is depicted in figure 7(*c*). Notably, the presence of a Prandtl–Meyer expansion fan connecting the supersonic flow states in regions (12) and (13), distinguishes this wave configuration from the four-wave configurations predicted by Vasilev *et al.* (2008).

The accurate prediction of the trajectories of TP_3 and IP_3 is essential for studying the triple-shock refraction. Figure 19 compares the trajectories of TP_3 and IP_3 between analytical and numerical results. The trajectory of TP_2 is also provided to emphasize its trajectory alteration upon encountering the interface. Notably, upon crossing the interface, the trajectory of the triple point undergoes a deflection towards the interface. This deflection becomes more apparent as Z_r increases. Consequently, with an increase in Z_r, a significant decrease is observed in the shock angle ($\beta_7(TP_3)$) of the transmitted Mach stem (MS_3) in the frame of reference attached to TP_3. Simultaneously, there is a corresponding increase in the oncoming flow Mach number ($M_{0'}(TP_3)$) upstream of the transmitted triple-shock configuration. The above analysis elucidates the underlying mechanism governing the disappearance of subsonic flow regions in the vicinity of TP_3 as Z_r increases, which is responsible for the formation of both the transmitted four-shock configuration and four-wave configuration.

Comparison of wave configurations immediately after the triple-shock refraction between the analytical predictions and numerical simulations is provided in figure 20.
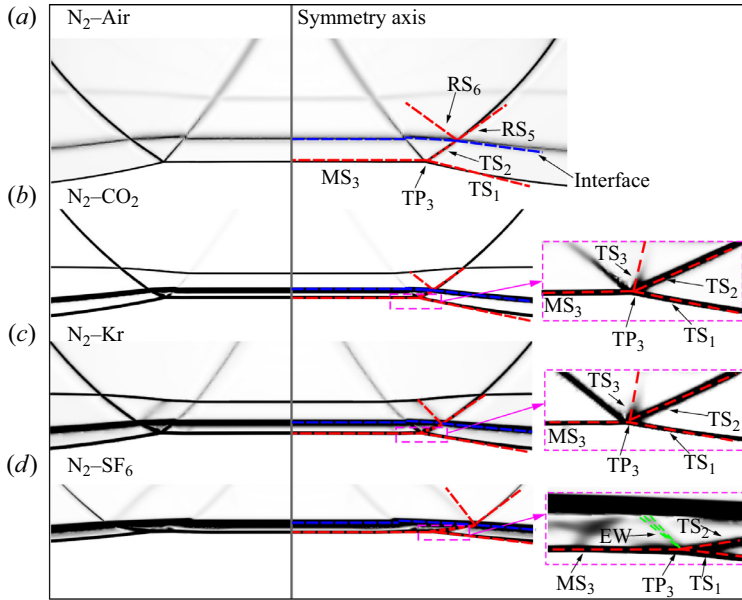
Figure 20. Comparison of wave configurations between analytical predictions (denoted by dashed lines) and numerical simulations.

The analytical wave configurations are denoted by dashed lines overlaid on the numerical schlieren images. The analytical model demonstrates exceptional capability in accurately predicting the configurations of transmitted waves. Consequently, the developed analytical model can also be utilized to assess the propagation of reverberation waves between interfaces in the case of RMI involving multiple interfaces.

As a final remark, the incident triple-shock configuration and initial interface examined in this paper are limited, which may not uncover all potential wave configurations, particularly those associated with irregular shock refraction and interaction. For each of the three patterns of triple-shock refraction identified in this paper, the shock-polar analysis provides information about the detailed wave configurations, and make it possible to identify the configuration of the transmitted waves. Furthermore, the different patterns of triple-shock refraction predicted by the shock polars are all verified experimentally and numerically. However, the criteria for determining which of those configurations will occur have not yet been established, but are the subject of ongoing research.

5. Conclusions

The refraction of an incident triple-shock configuration at planar fast–slow gas interfaces is investigated in this work. The incident triple-shock configuration is generated by diffracting a planar shock around a rigid cylinder, and four planar interfaces (N_2–air, N_2–Kr, N_2–CO_2 and N_2–SF_6) with varying acoustic impedance ratio (Z_r) being considered. The primary objective is to reveal the wave patterns and clarify the mechanisms that govern the deposition of circulation and velocity perturbation induced by triple-shock refraction.

The wave configurations associated with triple-shock refraction are investigated through shock tube experiments and numerical simulations. Depending on Z_r, an incident triple-shock configuration can be transmitted as either a triple-shock configuration,

a four-wave configuration or a four-shock configuration. To the authors' knowledge, such a four-shock configuration has not been previously reported. Subsequently, an analytical model describing triple-shock refraction is developed for the first time based on a gas dynamics approach. The analytical model demonstrates its capability in accurately predicting the resulting wave configurations from triple-shock refraction. Shock polar analysis reveals fundamental differences between the aforementioned four-wave configuration and those distinguished in Guderley reflection and Valisev reflection. Of great interest, the trajectory of the triple point exhibits a notable deflection towards the interface upon crossing it. Furthermore, a more pronounced deflection is observed for a larger Z_r, leading to a decrease in the shock angle of the transmitted Mach stem and simultaneously increasing upstream flow Mach number. This elucidates the underlying mechanism governing the disappearance of subsonic flow regions in the vicinity of the transmitted triple point as Z_r increases, which is responsible for the formation of both the transmitted four-shock and four-wave configurations.

One of the most significant contributions of this study is providing novel physical insights into the contributions of triple-shock refraction to the interface perturbation growth. The present investigation reveals that the reflected shock in an incident triple-shock configuration makes a significant negative contribution to both circulation deposition and velocity perturbation. Consequently, in cases of RM-like instability induced by a non-uniform shock with inherent triple-shock configurations, both the leading shock front and the reflected shocks travelling transversely behind it play crucial roles in the perturbation growth of the interface. This investigation sheds light on a puzzling phenomenon: the relatively insignificant contribution of baroclinic circulation to RM-like instability. Besides, this investigation also elucidates the underlying mechanism governing the reduction in growth rate of interface perturbation amplitude with increasing Atwood number. These findings are believed to be valuable for enhancing understanding and modelling of the RM-like instability.

Declaration of interests. The authors report no conflict of interest.

Author ORCIDs.

Ⓓ Enlai Zhang https://orcid.org/0000-0003-0066-7203;

Ⓓ Liyong Zou https://orcid.org/0000-0003-2702-1816;

Ⓓ Zhigang Zhai https://orcid.org/0000-0002-0094-5210.

References

ABD-EL-FATTAH, A.M. & HENDERSON, L.F. 1978*a* Shock waves at a fast-slow gas interface. *J. Fluid Mech.* **86** (1), 15–32.

ABD-EL-FATTAH, A.M. & HENDERSON, L.F. 1978*b* Shock waves at a slow-fast gas interface. *J. Fluid Mech.* **89** (1), 79–95.

ABD-EL-FATTAH, A.M., HENDERSON, L.F. & LOZZI, A. 1976 Precursor shock waves at a slow-fast gas interface. *J. Fluid Mech.* **76** (1), 157–176.

ANDERSON, J.D. JR. 2001 *Fundamentals of Aerodynamics*, 3rd edn. McGraw-Hill.

ARNETT, W.D., BAHCALL, J.N. & KIRSHNER, R.P. 1989 Supernova 1987A. *Annu. Rev. Astron. Astrophys.* **27**, 629–700.

BAI, C. & WU, Z. 2022 Type IV shock interaction with a two-branch structured transonic jet. *J. Fluid Mech.* **941**, A45.

BEN-DOR, G. 2007 *Shock Wave Reflection Phenomena*, 2nd edn. Springer.

BETTI, R. & HURRICANE, O.A. 2016 Inertial-confinement fusion with lasers. *Nat. Phys.* **12**, 435–448.

BROUILLETTE, M. 2002 The Richtmyer–Meshkov instability. *Annu. Rev. Fluid Mech.* **34**, 445–468.

BROWN, J.L. & RAVICHANDRAN, G. 2014 Analysis of oblique shock waves in solids using shock polars. *Shock Waves* **24**, 403–413.

BRYSON, A.E. & GROSS, R.W.F. 1961 Diffraction of strong shocks by cones, cylinders, and spheres. *J. Fluid Mech.* **10**, 1–16.

CHAUDHURI, A., HADJADJ, A. & CHINNAYYA, A. 2011 On the use of immersed boundary methods for shock/obstacle interactions. *J. Comput. Phys.* **230**, 1731–1748.

COLELLA, P. & HENDERSON, L.F. 1990 The von Neumann paradox for the diffraction of weak shock waves. *J. Fluid Mech.* **213**, 71–94.

GARDNER, J.H., BOOK, D.L. & BERNSTEIN, I.B. 1982 Stability of imploding shocks in the CCW approximation. *J. Fluid Mech.* **114**, 41–58.

GOUNKO, Y.P. 2017 Patterns of steady axisymmetric supersonic compression flows with a Mach disk. *Shock Waves* **27**, 495–506.

DE GOUVELLO, Y., DUTREUILH, M., GALLIER, S., MELGUIZO-GAVILANES, J. & MEVEL, R. 2021 Shock wave refraction patterns at a slow-fast gas-gas interface at superknock relevant conditions. *Phys. Fluids* **33**, 116101.

GUDERLEY, K.G. 1947 Considerations on the structure of mixed subsonic-supersonic flow patterns. *Tech. Rep.* Air Materiel Command Technical Report No. F-TR-2168-ND, ATI No. 22780. GS-AAF-Wright Field No. 39. U.S. Wright–Patterson Air Force Base.

HAWLEY, J.F. & ZABUSKY, N.J. 1989 Vortex paradigm for shock-accelerated density-stratified interfaces. *Phys. Rev. Lett.* **63** (12), 1241–1244.

HE, Y., PENG, N., LI, H., TIAN, B. & YANG, Y. 2023 Formation of the cavity on a planar interface subjected to a perturbed shock wave. *Phys. Rev. Fluids* **8**, 063402.

HENDERSON, L.F. 1966 The refraction of a plane shock wave at a gas interface. *J. Fluid Mech.* **26**, 607–637.

HENDERSON, L.F. 1989 On the refraction of shock waves. *J. Fluid Mech.* **198**, 365–386.

HENDERSON, L.F. 2014 The refraction of shock pairs. *Shock Waves* **24**, 553–572.

HENDERSON, L.F. & SIEGENTHALER, A. 1980 Experiments on the diffraction of weak blast waves: the von Neumann paradox. *Proc. R. Soc. Lond.* A **369**, 537–555.

HONG, L., BIN, Y., BIN, Z. & YANG, X. 2022 On mixing enhancement by secondary baroclinic vorticity in a shock-bubble interaction. *J. Fluid Mech.* **931**, A17.

ISHIZAKI, R. & NISHIHARA, K. 1997 Propagation of a rippled shock wave driven by nonuniform laser ablation. *Phys. Rev. Lett.* **78** (10), 1920–1923.

ISHIZAKI, R., NISHIHARA, K., SAKAGAMI, H. & UESHIMA, Y. 1996 Instability of a contact surface driven by a nonuniform shock wave. *Phys. Rev.* E **53** (6), R5592–R5595.

JAHN, R.G. 1956 The refraction of shock waves at a gaseous interface. *J. Fluid Mech.* **1** (5), 457–489.

JI, J., LI, Z., ZHANG, E., SI, D. & YANG, J. 2022 Intensification of non-uniformity in convergent near-conical hypersonic flow. *J. Fluid Mech.* **931**, A8.

JONES, M.A. & JACOBS, J.W. 1997 A membraneless experiment for the study of Richtmyer–Meshkov instability of a shock-accelerated gas interface. *Phys. Fluids* **9**, 3078–3085.

LAU-CHAPDELAINE, S.S.M. & RADULESCU, M.I. 2016 Viscous solution of the triple-shock reflection problem. *Shock Waves* **26**, 551–560.

LI, D., GUAN, B. & WANG, G. 2022*b* Effects of interface diffusion and shock strength on shock-accelerated SF_6 cylinder. *Phys. Fluids* **34**, 076109.

LI, D., WANG, G. & GUAN, B. 2019 On the circulation prediction of shock-accelerated elliptical heavy gas cylinders. *Phys. Fluids* **31**, 056104.

LI, J., DING, J., LUO, X. & ZOU, L. 2022*a* Instability of a heavy gas layer induced by a cylindrical convergent shock. *Phys. Fluids* **34**, 042123.

LI, Y., SAMTANEY, R. & WHEATLEY, V. 2018 The Richtmyer–Meshkov instability of a double-layer interface in convergent geometry with magnetohydrodynamics. *Matt. Radiat. Extremes* **3**, 207–218.

LIANG, Y., DING, J., ZHAI, Z., SI, T. & LUO, X. 2017 Interaction of cylindrically converging diffracted shock with uniform interface. *Phys. Fluids* **29**, 086101.

LIAO, S., ZHANG, W., CHEN, H., ZOU, L., LIU, J. & ZHENG, X. 2019 Atwood number effects on the instability of a uniform interface driven by a perturbed shock wave. *Phys. Rev.* E **99**, 013103.

LINDL, J.D., AMENDT, P., BERGER, R.L., GLENDINNING, S.G. & GLENZER, S.H. 2004 The physics basis for ignition using indirect-drive targets on the National Ignition Facility. *Phys. Plasmas* **11** (2), 339–491.

LIU, H., YU, B., CHEN, H., ZHANG, B. & LIU, H. 2020 Contribution of viscosity to the circulation deposition in the Richtmyer–Meshkov instability. *J. Fluid Mech.* **895**, A10.

LODATO, G., VERVISCH, L. & CLAVIN, P. 2016 Direct numerical simulation of shock wavy-wall interaction: analysis of cellular shock structures and flow patterns. *J. Fluid Mech.* **789**, 221–258.

MESHKOV, E.E. 1969 Instability of a shock wave accelerated interface between two gases. *Fluid Dyn.* **4**, 101–104.

MOSTERT, W., PULLIN, D.I., SAMTANEY, R. & WHEATLEY, V. 2018*a* Singularity formation on perturbed planar shock waves. *J. Fluid Mech.* **846**, 536–562.

MOSTERT, W., PULLIN, D.I., SAMTANEY, R. & WHEATLEY, V. 2018*b* Spontaneous singularity formation in converging cylindrical shock waves. *Phys. Rev. Fluids* **3**, 071401.

NISHIHARA, K., WOUCHUK, J.G., MATSUOKA, C., ISHIZAKI, R. & ZHAKHOVSKY, V.V. 2010 Richtmyer–Meshkov instability: theory of linear and nonlinear evolution. *Phil. Trans. R. Soc.* A **368**, 1769–1807.

NOURGALIEV, R.R., SUSHCHIKH, S.Y., DINH, T.N. & THEOFANOUS, T.G. 2005 Shock wave refraction patterns at interfaces. *Intl J. Multiphase Flow* **31**, 969–995.

OLEJNICZAK, J., WRIGHT, M.J. & CANDLER, G.V. 1997 Numerical study of inviscid shock interactions on double-wedge geometries. *J. Fluid Mech.* **352**, 1–25.

PELLONE, S., STEFANO, C.A.D., RASMUS, A.M., KURANZ, C.C. & JOHNSEN, E. 2021 Vortex-sheet modeling of hydrodynamic instabilities produced by an oblique shock interacting with a perturbed interface in the HED regime. *Phys. Plasmas* **28**, 022303.

PENG, G., ZABUSKY, N.J. & ZHANG, S. 2003 Vortex-accelerated secondary baroclinic vorticity deposition and late-intermediate time dynamics of a two-dimensional Richtmyer–Meshkov interface. *Phys. Fluids* **15** (12), 3730–3744.

PENG, N., YANG, Y., WU, J. & XIAO, Z. 2021 Mechanism and modelling of the secondary baroclinic vorticity in the Richtmyer–Meshkov instability. *J. Fluid Mech.* **911**, A56.

POLACHEK, H. & SEEGER, R.J. 1951 On shock-wave phenomena-refraction of shock waves at a gaseous interface. *Phys. Rev.* **84**, 922–929.

REN, Z., WANG, B., XIANG, G., ZHAO, D. & ZHENG, L. 2019 Supersonic spray combustion subject to scramjets: progress and challenges. *Prog. Aeronaut. Sci.* **105**, 40–59.

RICHTMYER, R.D. 1960 Taylor instability in shock acceleration of compressible fluids. *Commun. Pure Appl. Maths* **13**, 297–319.

SAMTANEY, R. & ZABUSKY, N.J. 1994 Circulation deposition on shock-accelerated planar and curved density-stratified interfaces: models and scaling laws. *J. Fluid Mech.* **269**, 45–78.

SKEWS, B.W. & ASHWORTH, J.T. 2005 The physical nature of weak shock wave reflection. *J. Fluid Mech.* **542**, 105–114.

SMALYUK, V.A. *et al.* 2020 Review of hydrodynamic instability experiments in inertially confined fusion implosions on National Ignition Facility. *Plasma Phys. Control Fusion* **62**, 014007.

SUN, M. & TAKAYAMA, K. 1999 Conservative smoothing on an adaptive quadrilateral grid. *J. Comput. Phys.* **150**, 143–180.

SUN, M. & TAKAYAMA, K. 2003 Vorticity production in shock diffraction. *J. Fluid Mech.* **478**, 237–256.

TAUB, A.H. 1947 Refraction of plane shock waves. *Phys. Rev.* **72**, 51–60.

THOMAS, V.A. & KARES, R.J. 2012 Drive asymmetry and the origin of turbulence in an ICF implosion. *Phys. Rev. Lett.* **109**, 075004.

TORO, E.F. 2009 The MUSCL-Hancock method. In *Riemann Solvers and Numerical Methods for Fluid Dynamics*, 3rd edn, pp. 429–432. Springer.

VASILEV, E.I. 1999 Four-wave scheme of weak Mach shock wave interaction under von Neumann paradox conditions. *Fluid Dyn.* **34**, 421–427.

VASILEV, E.I., ELPERIN, T. & BEN-DOR, G. 2008 Analytical reconsideration of the von Neumann paradox in the reflection of a shock wave over a wedge. *Phys. Fluids* **20**, 046101.

VELIKOVICH, A.L. 2000 Richtmyer–Meshkov-like instabilities and early-time perturbation growth in laser targets and Z-Pinch loads. *Phys. Plasmas* **7** (5), 1662–1671.

VELIKOVICH, A.L., SCHMITT, A.J., ZULICK, C., AGLITSKIY, Y., KARASIK, M., OBENSCHAIN, S.P., WOUCHUK, J.G. & COBOS CAMPOS, F. 2020 Multi-mode hydrodynamic evolution of perturbations seeded by isolated surface defects. *Phys. Plasmas* **27**, 102706.

VON NEUMANN, J. 1943 Oblique reflection of shock. *Tech. Rep.* Explos. Res. Rep. 12. Navy Department, Bureau of Ordinance, Washington, DC.

VON NEUMANN, J. 1945 Refraction, intersection and reflection of shock waves. *Tech. Rep.* NAVORD Rep. 203–245. Navy Department, Bureau of Ordinance, Washington, DC.

WAN, Q., JEON, H., DEITERDING, R. & ELIASSON, V. 2017 Numerical and experimental investigation of oblique shock wave reflection off a water wedge. *J. Fluid Mech.* **826**, 732–758.

WANG, H. & ZHAI, Z. 2020 On regular reflection to Mach reflection transition in inviscid flow for shock reflection ona convex or straight wedge. *J. Fluid Mech.* **884**, A27.

WANG, H., ZHAI, Z. & LUO, X. 2022 Prediction of triple point trajectory on two-dimensional unsteady shock reflection over single surfaces. *J. Fluid Mech.* **947**, A42.

WHITE, D.R. 1952 An experimental survey of the Mach reflection of shock waves. PhD thesis, Princeton University.

XIANG, G. & WANG, B. 2019 Theoretical and numerical studies on shock reflection at water/air two-phase interface: fast-slow case. *Intl J. Multiphase Flow* **114**, 219–228.

YANG, J., KUBOTA, T. & ZUKOSKI, E.E. 1994 A model for characterization of a vortex pair formed by shock passage over a light-gas inhomogeneity. *J. Fluid Mech.* **258**, 217–244.

YANG, X., CHERN, I., ZABUSKY, N.J., SAMTANEY, R. & HAWLEY, J.F. 1992 Vorticity generation and evolution in shock-accelerated density-stratified interfaces. *Phys. Fluids* A **4**, 1531–1540.

YANG, Y., LI, S. & WU, Z. 2013 Shock reflection in the presence of an upstream expansion wave and a downstream shock wave. *J. Fluid Mech.* **735**, 61–90.

ZABUSKY, N.J. 1999 Vortex paradigm for accelerated inhomogeneous flows: visiometrics for the Rayleigh–Taylor and Richtmyer–Meshkov environments. *Annu. Rev. Fluid Mech.* **31**, 495–536.

ZASLAVSKY, B.I. & SAFAROV, P.A. 1975 Mach reflection of weak shock waves from a rigid wall. *J. Appl. Mech. Tech. Phys.* **14** (5), 624–629.

ZHAI, Z., LI, W., SI, T., LUO, X., YANG, J. & LU, X. 2017 Refraction of cylindrical converging shock wave at an air/helium gaseous interface. *Phys. Fluids* **29**, 016102.

ZHAI, Z., LIANG, Y., LIU, L., DING, J., LUO, X. & ZOU, L. 2018 Interaction of rippled shock wave with fast-slow interface. *Phys. Fluids* **30**, 046104.

ZHAI, Z., SI, T., LUO, X. & YANG, J. 2011 On the evolution of spherical gas interfaces accelerated by a planar shock wave. *Phys. Fluids* **23**, 084104.

ZHANG, E., LI, Z., JI, J., SI, D. & YANG, J. 2021 Converging near-elliptic shock waves. *J. Fluid Mech.* **909**, A2.

ZHOU, Y. 2017*a* Rayleigh–Taylor and Richtmyer–Meshkov instability induced flow, turbulence, and mixing. I. *Phys. Rep.* **720–722**, 1–136.

ZHOU, Y. 2017*b* Rayleigh–Taylor and Richtmyer–Meshkov instability induced flow, turbulence, and mixing. II. *Phys. Rep.* **723–725**, 1–160.

ZOU, L., AL-MAROUF, M., CHENG, W., SAMTANEY, R. & LUO, X. 2019 Richtmyer–Meshkov instability of an unperturbed interface subjected to a diffracted convergent shock. *J. Fluid Mech.* **879**, 448–467.

ZOU, L., LIU, J., LIAO, S., ZHENG, X., ZHAI, Z. & LUO, X. 2017 Richtmyer–Meshkov instability of a flat interface subjected to a rippled shock wave. *Phys. Rev.* E **95**, 013107.